Mechanics of Materials 179 (2023) 104600

Contents lists available at ScienceDirect

Mechanics of Materials

journal homepage: www.elsevier.com/locate/mechmat

Influence of uniform temperature variations on hybrid bonded joints with a circular or tubular cross-sectional area

Hugo C. Biscaia [a,b,*], Ana P. Martins [a], Wan-Yang Gao [c], Marta S. Carvalho [a,b]

[a] UNIDEMI and Department of Mechanical and Industrial Engineering, NOVA School of Science and Technology, 2829-516, Caparica, Portugal
[b] Laboratório Associado de Sistemas Inteligentes, LASI, 4800-058 Guimarães, Portugal
[c] State Key Laboratory of Ocean Engineering, School of Naval Architecture, Ocean and Civil Engineering, Shanghai Jiao Tong University, Shanghai, 200240, China

ARTICLE INFO

Keywords:
CFRP
Metallic structures
Thermal loading
Analytical approach
Tubular joints

ABSTRACT

The use of lightweight structures is a current concern in several engineering domains. To obtain such types of structures, the bonding technique using Carbon Fibre-Reinforced Polymers (CFRP) has been most recently considered a primary option. If CFRP is known to have a high strength-to-weight ratio or high corrosion resistance, the bonding technique does not need to add other fixation components and it also prevents stress concentrations. However, when combined with, e.g. a metallic surface, the high difference between the thermal expansion coefficient of the CFRP composite and the metallic material may raise some issues when the adhesively bonded structure is subjected to thermal loading. Therefore, the present work presents an analytical model that facilitates the comprehension of the impact of temperature on a hybrid bonded joint with a circular or tubular cross-sectional area. The full debonding process of a double but bonded joint with a regular curvature is discussed thoroughly. Due to the susceptibility of current adhesives to lose their mechanical properties for relatively high temperatures, the vitreous transition temperature of the adhesives and their influence on the local adhesive model is considered in a deeper analysis. The Finite Element Method (FEM) was used to validate all the derived analytical equations, which were achieved due to the close predictions obtained from both ways, i.e. from the numerical simulations and the proposed closed-form solutions.

1. Introduction

With successive engineering advances, the construction of new structures in different industry sectors has been responding to new social requirements such as the use of raw materials in a rational way for a long-term duration and without forgetting its aesthetics. In this way, and due to their appealing properties, the use of Carbon Fibre-Reinforced Polymers (CFRP) in different applications in the civil construction, automotive, naval, and aerospace industry has increased. Several examples can be found in the literature (Lu et al., 2007; Valluzzi et al., 2007; Mostofinejad and Shameli, 2013; Sahin and Dawood, 2016; Ferreira et al., 2016; Biscaia et al., 2017a; Siddika et al., 2019; Lee and Lopez, 2020; Pangestuti et al., 2020; Moshiri et al., 2020) where CFRP composites are being bonded to another material, resulting in a durable and lightweight structure with a high-strength performance. However, the integrity of these structures depends on the joining technique's success and their performance during their serviceability period. The main advantage of the bonding technique is that it allows us to create an overlapped bonded area where the developed stress distribution is uniform that otherwise would not be possible to obtain. In the automotive industry, for instance, the use of adhesives rather than other mechanical fixations allows the constructors to decrease the final weight of the vehicle. Under these circumstances, Benedyk (2010) has estimated that for every 10% reduction in the mass of the vehicle, a saving of approximately 6%–8% of fuel consumption is achieved. Consequently, the vehicle has lower carbon dioxide emissions to the atmosphere, which makes the vehicle friendlier to the environment.

However, the adhesives used to bond two materials (or adherends) and build a hybrid bonded joint are quite susceptible to high temperatures due to the loss of their initial mechanical properties (Leone et al., 2009; Biscaia et al., 2017b; Biscaia and Ribeiro, 2019; Zhou et al., 2020; He et al., 2020; Lye et al., 2021). With the temperature increase, the adhesives, usually epoxy resin, shift from their initial glassy state to a rubbery and softened state, which is followed by an efficiency decrease of the adhesive on transferring the stresses within the joint and between materials. Thereby, the so-called vitreous (or glass) transition

* Corresponding author.
E-mail address: hb@fct.unl.pt (H.C. Biscaia).

https://doi.org/10.1016/j.mechmat.2023.104600
Received 23 July 2022; Received in revised form 24 January 2023; Accepted 13 February 2023
Available online 16 February 2023

temperature (T_g) of the adhesives has a relevant impact on the bond performance of an overlapped bonded joint subjected to thermal loading. Comparing this scenario with the shrinkage of the adhesive during its curing period, the induced interfacial stresses due to thermal expansion are much more significant than the ones obtained from the adhesive shrinkage (Da Silva, 2010). Therefore, the correct prediction of the thermal expansion stresses of an overlapped bonded joint has extreme importance for anyone who needs to design these joints under thermal loading. To help on such task, numerous experiments have been carried out by several researchers, e.g. (Nozaka et al., 2005; Xia and Teng, 2005; Lam et al., 2008; Borrie et al., 2015; He and Xian, 2016; Yang et al., 2017, 2019a, 2019b; Heshmati et al., 2017; Doroudi et al., 2019; Zhou et al., 2019; Hu and Jiang, 2019; Saleh et al., 2020), where, in most of the cases, single or double-bonded joints were used to analyze the bond performance of hybrid bonded joints, such as those where CFRP composites are externally bonded onto a metallic and flat plate. Adhesives have, therefore, a critical key role in the joining success but due to their variety available in the market, it makes it difficult to understand the bond behaviour of different overlapped bonded joints. For instance, their strength and strain energy are highly dependent on the chemical structure of the polymer chains that form the adhesive, and consequently, the bonds in the polymer chain vary from covalent intermolecular bonds to other weaker bonds such as van der Waals, hydrogen, or ionic bonds (Zhou et al., 2020). With the increase in temperature, these bonds lose their initial strengths in different ways which lead researchers to focus on the determination of T_g and fixing its value as the one beyond which the allowable service conditions for the overlapped bonded joints cannot be ensured anymore.

In the case of some industries sectors such as the civil construction sector, the adhesives used have a short curing time in which the adhesives reach some satisfactory mechanical properties under ambient temperature while in other industries such as the automotive or naval industries, the adhesives can be cured within a more controlled environment and longer curing period. Consequently, the adhesives often used in civil construction have a T_g that barely exceeds approximately 60 °C (Zhou et al., 2020; Corcione et al., 2014) whilst in the naval industry sector, the values of T_g may reach an interval between approximately 190 °C to 240 °C (Biscaia, 2019, 2020). Then, the bond performance of an overlapped bonded joint may have more or less relevance depending on which industry sector it is inserted into.

To facilitate its design, the Finite Element Method (FEM) is a good tool to simulate the bond behaviour of different bonded joints in which the so-called Cohesive Zone Modelling (CZM) can be applied. However, the exact quantification of the cohesive models considering the influence of temperature still requires, in most of the cases, experimental data. Therefore, there are no other alternatives to the use of existing models available in the literature, e.g. (Biscaia and Ribeiro, 2019; Dong and Hu, 2016; Dai et al., 2013), which may be not adequate for the problem under design. The aim of using cohesive models is to locally describe the bond performance between two (equal or not) materials, and most engineering problems, require the use of complex cohesive models with the ability to deal also with a mixed fracture situation within an uncouple or couple way (Biscaia et al., 2017b; Tvergaard, 1990; Kafkalidis and Thouless, 2002; Li et al., 2006; Van den Bosch et al., 2006; De Lorenzis and Zavarise, 2008). However, in some simple cases where one of the fracture modes is isolated, the cohesive models can be defined through only one model that tries to reproduce the bond behaviour of the bonded joint. For instance, in a problem where the ruptures are expected to be coincident with a pure fracture Mode II (sliding mode), the bond stress *vs.* interfacial slip relationship is commonly used (Lee and Lopez, 2020; Dai et al., 2005; Zhou et al., 2010; Liu and Wu, 2012; Wu and Jiang, 2013; Fernando et al., 2014; Biscaia et al., 2015a; Wang et al., 2016). In this case, the interfacial bond stresses developed within the bonded area have the same direction as the loads transmitted to the bonded joint. In the direction consistent with fracture Mode III, the same bond stress *vs.* interfacial slip relationship defined for Mode II has been used also for this Mode III (Biscaia et al., 2013a, 2013b). In Mode I, the interfacial stresses develop perpendicularly to the bonded area, and if they correspond to a tensioned situation that leads to interfacial peeling stresses, the strength of the bonded joint decreases abruptly (Biscaia et al., 2015a; Neto et al., 2016; Biscaia and Chastre, 2018). Otherwise, the strength of the bonded joints increases when under compression (Biscaia et al., 2015a; Biscaia and Chastre, 2018).

Although some studies can be found in the literature, e.g. (Biscaia et al., 2017b; Biscaia and Ribeiro, 2019; Zhou et al., 2020; He et al., 2020; Lye et al., 2021; Da Silva, 2010; Yang et al., 2019a; Biscaia, 2019, 2020; Li et al., 2016a), where the influence of the temperature variations on flat overlapped bonded joints is analysed under Mode II, this is a subject that needs to be better understood when applied, for instance, on tensioned members of trusses (Qiu et al., 2017). In such cases, the joints of tubular CFRP composites localized on the truss knots are crucial for the integrity of the truss. For this reason, the main purpose of this work is to analyze the bond behaviour of overlapped bonded joints with a circular curvature when subjected to a temperature variation. Since from a practical point of view, the use of analytical formulations is preferred over numerical and more sophisticated ones, the present work introduces a relatively simple closed-form solution that allows us to fully describe the debonding process of a hybrid overlapped bonded joint with a circular curvature under temperature variations. To validate the proposed analytical model, the analytical results are confronted against the results obtained from a FE analysis. To numerically model the contact between bonded materials, the CZM is used. Several models were developed to simulate the bond behaviour of different overlapped joints with different geometries and covering, therefore, a wider range of circular or tubular hybrid bonded joints under different temperature variations. Based on both results, analytical and numerical, a good agreement could be observed whether on the predictive of the debonding states of the overlapped joints or the temperature *vs.* interfacial slip relationship (ΔT *vs.* s). Moreover, for the randomly selected temperature magnitudes within each debonding state, the analytical proposed model was able to track very closely the numerical results, namely the interfacial slips or stresses developed throughout the overlapped bonded length, or the strains developed in both materials.

2. Proposed analytical model

2.1. Basic assumptions

Before introducing it, it is important to clarify which assumptions the proposed analytical model is based on. No less important is the definition of the shape used to locally model the bond behaviour between materials as well as the influence that a temperature variation may locally cause within the bonded interface. Only based on these two main aspects, it would be possible to identify and make a full description of the debonding process of a hybrid overlapped bonded joint whether with a circular, tubular or a simple flat cross-sectional area.

In the definition of the adhesive model, depending on the materials used in the bonded joint, the choice of the more appropriate adhesive model will fall into the one that can better represent the relationship between the bond stresses and the interfacial slips. For instance, to locally reproduce the bond behaviour between a CFRP externally bonded onto a concrete surface, exponential adhesive models seem to be more appropriate due to the cracking of concrete (Biscaia et al., 2016), whereas the bilinear or trapezoidal models may better describe the local bond behaviour between, e.g., a CFRP externally bonded onto a steel plate with a stiff or ductile adhesive, respectively (Fernando et al., 2014; Wang et al., 2016; Biscaia et al., 2016; He et al., 2021). Nevertheless, there are several studies, e.g. (Li et al., 2018a; Lu et al., 2005; Elsayed et al., 2006) where the authors have used the bilinear adhesive model to locally approximate the bond behaviour of CFRP-to-concrete joints. Thereby, the bilinear adhesive model is a well-known model but unlike

concrete, steel does not crack and for this reason, it is more suitable for use on CFRP-to-metal joints.

The influence of the temperature on the adhesives is the second main aspect to be considered here. As the temperature in the hybrid bonded joint reaches a value close to the vitreous transition temperature (T_g) of the adhesive, the initial mechanical properties of the adhesive tend to degrade and the initial effectiveness of the adhesive in transferring stresses between materials is severely affected. To follow such interfacial degradation, the initial parameters that define the local adhesive model must change with temperature. Therefore, the local adhesive model should reflect, in a realistic way, all those changes. In the case of flat CFRP-to-steel bonded joints, the authors have already proposed a pure Mode II temperature-dependent adhesive model elsewhere (Biscaia and Ribeiro, 2019). Since it was adopted in the present work, a brief explanation of this model (Biscaia and Ribeiro, 2019) is given in the next subsection.

For all the previous explanations, the bilinear adhesive model shown in Fig. 1 was selected and used in the current work to predict the bond performance of hybrid overlapped bond joints with a circular or tubular cross-sectional area. To allow the full description of the debonding process of these types of joints subjected to temperature changes, the influence of T_g on the adhesive is ignored. However, the temperature-dependent adhesive model in (Biscaia and Ribeiro, 2019) can be implemented in the proposed analytical model and the influence of T_g can be considered during the debonding process of the hybrid bonded joint. In addition, and for the sake of the simplicity of the analytical solutions herein derived, the following aspects were also considered in the proposed analytical model:

(i) the thicknesses of the bonded materials remain unchanged with the thermal loading;
(ii) the dilatation or contraction of the materials due to, respectively, very high or very low temperatures are ignored;
(iii) the temperature variation will have a uniform distribution through the thicknesses of the materials which, from a practical point of view, may fall into hybrid bonded joints where both materials have thin thicknesses;
(iv) the local bond behaviour between materials is controlled by a bilinear adhesion model with a temperature dependency (see Fig. 2);
(v) in the same cross-section of the hybrid bonded joint, the developed interfacial slips are the same which implies that the bond stresses are also the same along an angle θ that is made by the arc at the centre of the circular cross-section of the overlapped bonded joint;
(vi) although the thermal loading may influence the elastic modulus of the bonded materials, these were kept unchanged during the full description of the debonding process of the hybrid bonded joint. However, like the influence of T_g that can be implemented and considered in the current proposed analytical model, the changes in the elastic modulus of both materials can be also implemented and considered in the analytical model;
(vii) based on the bilinear adhesive model, the hybrid overlapped bonded joint will undergo the following three stages: Elastic (E); Softening (S); and Debonded (D) (see Fig. 1). Therefore, the states that the overlapped bonded joint will undergo during its debonding process will include, whether in an isolated or combined way, those three stages.

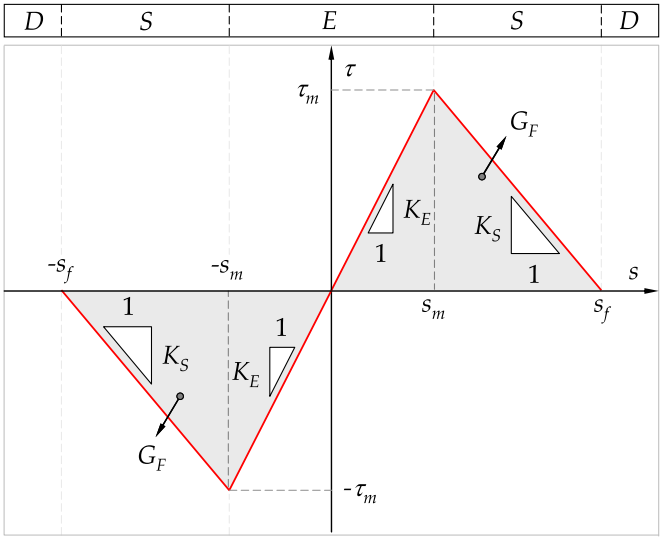

Fig. 1. Adopted bilinear adhesion model.

2.2. The temperature-dependent adhesive model

To give an overview of the main aspects that support the temperature-dependent adhesive model adopted in this work, a brief explanation is presented next. Nevertheless, the reading of the original work (Biscaia and Ribeiro, 2019) is suggested that the reader may find further and more detailed explanations.

This model is based on three main parameters that change according to the magnitude of the temperature: (i) elastic stiffness (K_E); softening stiffness (K_S); and (iii) fracture energy (G_F). The first one defines the changes that will occur in the Elastic (E) stage of the adhesive model, whereas the second one describes the changes within the softening (S) stage (see Fig. 2a). The third one aims to control the changes in the energy released during the debonding process per a unit area of the overlapped length with the temperature. The adhesive model is based on several tests which define the changes occurring in the initial values of K_E, K_S, and G_F. The quantification of these changes due to the thermal loading was calibrated with the experimental available data in the literature (Biscaia and Ribeiro, 2019; Al-Shawaf et al., 2006, 2009; Al-Shawaf, 2010; Nguyen et al., 2011a; Abed, 2012; Liu et al., 2014; Li et al., 2016b, 2018b; Zhou et al., 2017) and the following ratios $K_E(T)/K_E$, $K_S(T)/K_S$, and $G_F(T)/G_F$ were obtained:

$$\frac{K_E(T)}{K_E} = 1 - \frac{1}{1 + e^{-k_{e1}\cdot\left(\frac{T}{T_g} - k_{e2}\right)}} \tag{1}$$

$$\frac{K_S(T)}{K_S} = 1 - \frac{1}{1 + e^{-k_{s1}\cdot\left(\frac{T}{T_g} - k_{s2}\right)}} \tag{2}$$

and

$$\frac{G_F(T)}{G_F} = 1 - \frac{1}{1 + e^{-g_1\cdot\left(\frac{T}{T_g} - g_2\right)}} \tag{3}$$

where $K_E(T)$ and $K_S(T)$ are the elastic and the softening stiffnesses at temperature T, respectively; $G_F(T)$ is the Mode II fracture energy at temperature T; and k_{e1}, k_{e2}, k_{s1}, k_{s2}, g_1, and g_2 are all dimensionless parameters obtained from the same minimization process where Eq. (1) to Eq. (3) were adjusted to the experimental data. If in the case of Eq. (1) and Eq. (3) a decrease in the initial values due to the increase in temperature can be noticed clearly, the results supporting Eq. (2) were scattered. Still, considering the data used in the original work (Biscaia and Ribeiro, 2019), it seems to be reasonable to assume that the initial softening stiffness K_S tends to decrease with the increase in temperature as well. Thus, and in the absence of more experimental data to refine the model, the values of those dimensionless parameters are $k_{e1} = 4.953$, $k_{e2} = 1.000$, $k_{s1} = 6.401$; $k_{s2} = 1.000$, $g_1 = 10.176$ and $g_2 = 1.107$ (Biscaia and Ribeiro, 2019).

The complete definition of the bilinear adhesive model is made

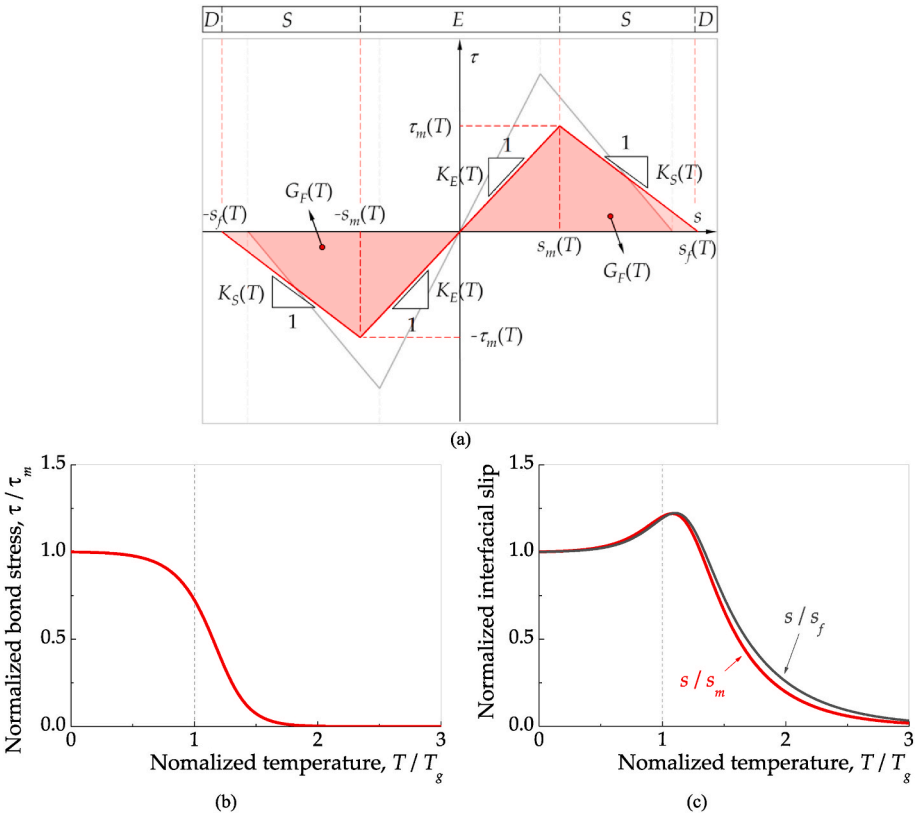

Fig. 2. Influence of the thermal loading in the: (a) bilinear adhesive model proposed in (Biscaia and Ribeiro, 2019); (b) maximum interfacial stress (τ_m); and (c) interfacial slips s_m and s_f.

through the quantification of the maximum interfacial stress and its corresponding interfacial slip at temperature T, as well as the quantification of the interfacial slip beyond which both materials begin to separate from each other at temperature T, i.e. (Biscaia and Ribeiro, 2019):

$$\tau_m(T) = \sqrt{\frac{2G_F(T)\cdot K_E(T)\cdot K_S(T)}{K_E(T)+K_S(T)}} \tag{4}$$

$$s_m(T) = \sqrt{\frac{2G_F(T)\cdot K_S(T)}{K_E(T)\cdot[K_E(T)+K_S(T)]}} \tag{5}$$

and

$$s_f(T) = \sqrt{\frac{2G_F(T)\cdot[K_E(T)+K_S(T)]}{K_E(T)\cdot K_S(T)}} \tag{6}$$

Fig. 2b and c show the changes in τ_m, s_m, and s_f due to the temperature increase predicted by the temperature-dependent adhesive model in (Biscaia and Ribeiro, 2019). From Fig. 2a, it can be seen that as the temperature becomes closer to T_g, the maximum interfacial stress decays abruptly. For instance, when $T = T_g$, the initial value of τ_m is reduced by approximately 38%. In the case of the interfacial slips, the increase of the temperature seems to increase the interfacial slips also. However, a peak on the interfacial slips is obtained at a temperature magnitude slightly higher than T_g, after which, the interfacial slips tend to decrease. Despite the model has been calibrated with extensive experimental data, this can be explained by the increase of the effective bond length, i.e. the length beyond which the load capacity, with the temperature increase (Biscaia and Ribeiro, 2019; Nguyen et al., 2011b, 2011c; Zhao et al., 2014). Thus, with the increase of the temperature, the effective bond length largely increases, and to obtain the local adhesive model of the joint, a longer overlapped bonded joint is needed. However, this is not usually ensured due to the limitations of the available testing equipment that limits the dimension of the specimens. At an elevated temperature level, the initial overlapped bonded length becomes too short which inverts, therefore, the initial trend of increasing interfacial slips observed in Fig. 2b with the temperature, and begins to decrease (Biscaia and Ribeiro, 2019).

2.3. Equilibrium equations

To obtain the equilibrium equations it is first considered a finite length dx of the curved overlapped bonded joint is shown in Fig. 3. From the equilibrium of the forces in the finite length dx, the following equations can be obtained:

$$\sigma_{1,x} - \frac{2\tau\cdot(R-t_1)}{t_1\cdot(2R-t_1)} = 0 \tag{7}$$

and

$$\sigma_{2,x} + \frac{2\tau\cdot(R-t_1)}{t_2\cdot(2R-2t_1-t_2)} = 0 \tag{8}$$

where $\sigma 1,x$ and $\sigma 2,x$ are the first derivative with respect to x (i.e. the axis parallel with the overlapped bonded length) of the normal stresses in material 1 and 2, respectively; t_1 and t_2 are the thicknesses of material 1 and material 2, respectively; R is the external radius curvature of the cross-sectional area of the tubular bonded hybrid transition; and τ is the interfacial bond stress. Since Eq. (7) or (8) have no dependencies on the angle θ, these can be applied to cross-sectional transitions bonded joints with either circular or tubular sections. Moreover, the debonding phenomenon of a circular or tubular hybrid transition joint can be analysed through a single line parallel with the overlapped bonded length. It should be also mentioned that if a flat bonded joint is considered, the external radius curvature R in Eqs. (7) and (8) assume an infinite which

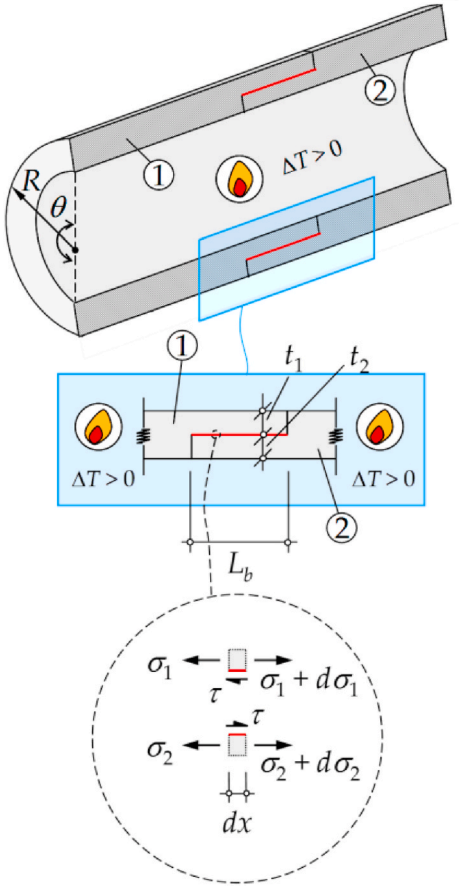

Fig. 3. Equilibrium of the forces in a tubular cross-sectional hybrid bonded joint with a double butt lap configuration.

leads, respectively, to the two following equations:

$$\sigma_{1,x} - \frac{\tau}{t_1} = 0 \tag{9}$$

and

$$\sigma_{2,x} + \frac{\tau}{t_2} = 0. \tag{10}$$

These two equations, Eqs. (9) and (10), are the same equilibrium equations that would be obtained from a flat hybrid bonded joint in which both materials had the same width.

In addition to Eqs. (7) and (8) and under thermal loading, the forces developed in both materials are auto-equilibrated, and therefore, at any point of the overlapped bonded joint, the following equation can be established also:

$$F_1 + F_2 = 0 \tag{11}$$

where F_1 and F_2 are the axial forces in materials 1 and 2, respectively.

2.4. Axial stresses and strain equations

As already mentioned, assuming that the hybrid transition bonded joint is carried out by two materials with an elastic behaviour, the stresses in both materials, material 1 and material 2, are, respectively:

$$\sigma_1 = E_1 \cdot \varepsilon_1 \tag{12}$$

and

$$\sigma_2 = E_2 \cdot \varepsilon_2 \tag{13}$$

where E_1 and E_2 are the elastic modulus of material 1 and material 2, respectively; and $\varepsilon_{1,x}$ and $\varepsilon_{2,x}$ are the total strains in material 1 and material 2. In the present conditions, these two strains can be respectively defined according to:

$$\varepsilon_1 = u_{1,x} - \alpha_1 \cdot \Delta T \tag{14}$$

and

$$\varepsilon_2 = u_{2,x} - \alpha_2 \cdot \Delta T \tag{15}$$

where α_1 and α_2 are the linear thermal expansion coefficients of material 1 and material 2, respectively; $u_{1,x}$ and $u_{2,x}$ correspond to the first derivatives of the displacements in materials 1 and 2, respectively, with respect to x in which the x-axis is parallel with the overlapped length; and ΔT is the temperature variation (corresponding to the thermal loading), which is defined by the amplitude between the final and initial temperatures, i.e.:

$$\Delta T = T_f - T_i \tag{16}$$

where T_f and T_i are the final and the initial temperatures, respectively. Introducing Eq. (14) into Eq. (12) the stresses in material 1 are:

$$\sigma_1 = E_1 \cdot \left(u_{1,x} - \alpha_1 \cdot \Delta T\right) \tag{17}$$

whilst introducing Eq. (15) into Eq. (13), the stresses in material 2 are:

$$\sigma_2 = E_2 \cdot \left(u_{2,x} - \alpha_2 \cdot \Delta T\right) \tag{18}$$

Denoting the interfacial slips (s) as the relative displacements between material 1 and material 2, i.e.:

$$s = u_1 - u_2 \tag{19}$$

when its first derivative with respect to x is introduced in (18), it yields:

$$\sigma_1 = E_1 \cdot \left(u_{2,x} + s_{,x} - \alpha_1 \cdot \Delta T\right) \tag{20}$$

and

$$\sigma_2 = E_2 \cdot \left(u_{1,x} - s_{,x} - \alpha_2 \cdot \Delta T\right) \tag{21}$$

Isolating $u_{1,x}$ in Eq. (21), we have:

$$u_{1,x} = \frac{\sigma_2}{E_2} + s_{,x} + \alpha_2 \cdot \Delta T \tag{22}$$

which, when introduced into Eq. (17), leads to:

$$s_{,x} = \frac{\sigma_1}{E_1} - \frac{\sigma_2}{E_2} + (\alpha_1 - \alpha_2) \cdot \Delta T \tag{23}$$

which can be rewritten as follows:

$$s_{,x} = \frac{F_1}{E_1 A_1} - \frac{F_2}{E_2 A_2} + (\alpha_1 - \alpha_2) \cdot \Delta T \tag{24}$$

where A_1 and A_2 are the cross-sectional areas of materials 1 and 2, respectively, i.e.:

$$A_1 = \frac{\theta}{2} t_1 \cdot (2R - t_1) \tag{25}$$

and

$$A_2 = \frac{\theta}{2} t_2 \cdot (2R - 2t_1 - t_2) \tag{26}$$

where t_1 and t_2 are the thicknesses of material 1 and material 2, respectively; and θ is the angle (in radians) made by the arc at the centre of the circular cross-section of the overlapped bonded joint (see Fig. 3). Introducing now Eq. (11) into Eq. (24), we have:

$$\sigma_1 = \frac{E_1}{1+r}\cdot\left[s_{,x} - (\alpha_1 - \alpha_2)\cdot\Delta T\right] \tag{27}$$

where r is defined as the ratio between the axial stiffnesses of material 1 and material 2, i.e.:

$$r = \frac{E_1 A_1}{E_2 A_2} \tag{28}$$

or, considering Eqs. (25) and (26):

$$r = \frac{E_1 t_1}{E_2 t_2}\cdot\frac{2R - t_1}{2R - 2t_1 - t_2} \tag{29}$$

On the other hand, the stresses in material 2 can be calculated if in Eq. (11) it is introduced Eq. (27) which, after a few simple mathematical operations, gives:

$$\sigma_2 = -\frac{r\cdot E_2}{1+r}\cdot\left[s_{,x} - (\alpha_1 - \alpha_2)\cdot\Delta T\right] \tag{30}$$

The determinations of the strains developed in both materials are now determined. Hence, for the calculation of the strains in material 1, Eq. (27) is introduced into Eq. (14), which gives:

$$u_{1,x} = \frac{1}{1+r}\cdot\left[s_{,x} - (\alpha_1 - \alpha_2)\cdot\Delta T\right] + \alpha_1\cdot\Delta T \tag{31}$$

The strains developed in material 2 can be calculated if Eq. (30) is introduced into Eq. (18). Thus, the following equation is derived:

$$u_{2,x} = -\frac{r}{1+r}\cdot\left[s_{,x} - (\alpha_1 - \alpha_2)\cdot\Delta T\right] + \alpha_2\cdot\Delta T \tag{32}$$

Particularly Eq. (31) is quite useful since, during an experimental test, it allows the calculations of the interfacial slips throughout the overlapped bonded length. So, to calculate the interfacial slips, the integration of the following equation can be carried out:

$$s_{,x} = (1+r)\cdot u_{1,x} - (r\cdot\alpha_1 + \alpha_2)\cdot\Delta T \tag{33}$$

Another interesting aspect derived from Eq. (33) is the influence of the temperature variations on the interfacial slips which are directly proportional with $r\bullet\alpha_1 + \alpha_2$. The interfacial slips are also magnified when $r = 1$, i.e. when the axial stiffness of both materials has the same value. However, with no temperature variation and in the presence of a rigid material 2 ($r = 0$), Eq. (33) is reduced to

$$s_{,x} = u_{1,x} \tag{34}$$

which is a very well-known relationship used in the literature by several authors, e.g. (Focacci et al., 2000; Khalfallah, 2008; Shi et al., 2013; Vaculik et al., 2018; Zhu et al., 2020; Biscaia and Diogo, 2020), to calculate the strains developed in FRP composites bonded onto a concrete and rigid substrate.

2.5. Governing equation

The temperature variations herein considered lead to a uniform distribution throughout the thicknesses of material 1 and material 2. Under this condition, the derivative of Eq. (23) with respect to x, leads to:

$$s_{,xx} = \frac{\sigma_{1,x}}{E_1} - \frac{\sigma_{2,x}}{E_2} \tag{35}$$

which introducing (7) and (8) into (25), gives the following equilibrium differential equation of the overlapped hybrid bonded joint with a regular curvature:

$$s_{,xx} - \lambda\cdot\tau = 0 \tag{36}$$

where

$$\lambda = \frac{2(R - t_1)}{(2R - t_1)\cdot E_1 t_1}\cdot(1+r) \tag{37}$$

Taking a deep look into Eq. (37) it can be stated that parameter λ should vary between a minimum and a maximum value. The latter will be obtained when

$$R = t_1 + t_2 \tag{38}$$

and it represents a circular section with no hollows in it whereas the former one is obtained when $R \to \infty$, which leads to:

$$\lambda = \frac{1}{E_2 t_2} + \frac{1}{E_1 t_1} \tag{39}$$

and it is associated with flat adhesively bonded structures. Thus, to describe the debonding process of a hybrid overlapped bonded joint with a circular or tubular cross-sectional area, Eq. (36) should be solved for each state that the interface will undergo until the complete separation of material 1 from material 2. These states will depend on the three stages already defined for the bi-linear adhesive model: Elastic (E); Softening (S) and Debonded (D). In the following section, the analyses of all the states that the hybrid overlapped bonded joint will undergo until its complete debonding due to the thermal loading are described and explained next.

3. Definition of the debonding process

The identification, description, and definition of each state that the hybrid overlapped bonded joint undergoes during the thermal loading until its complete debonding are presented thoroughly. Before entering into further details, it should be bear in mind first that a temperature variation leads to a symmetric condition to the overlapped length. Therefore, the mid-point of the hybrid overlapped bonded joint cannot slip and, consequently, in the exclusive presence of thermal loading, the elastic and softened regions of the overlapped bonded length will never disappear during the debonding process of the joint. Regarding the adhesive model, all points of the overlapped bonded length should follow the interfacial stress *vs.* slip relationship defined there. Since at the centre of the overlapped length the interfacial slips are zero, the centre of the overlapped length will remain in the E state. Other regions next to this E region, will be softened and at the vicinities of both ends of the joint will occur the separation (or debonding) of material 1 from material 2. Naturally, as the debonding limits increase, the E and S regions decrease but, from a theoretical perspective, both will never disappear. It is important to also mention that to fully describe the debonding process of a hybrid overlapped bonded length subjected to thermal loading, the influence of T_g on the adhesive is not considered. Still, this does not limit the proposed analytical model to such an unrealistic situation as it will be shown later.

In the subsequent sections, each state that the overlapped bonded joint will undergo during its debonding process is described through the definition of the interfacial slips, stresses, and strains developed in both materials, 1 and 2. All the states are presented here in their order of appearance in the debonding process: (i) Elastic (E) state; (ii) Softening-Elastic-Softening (S-E-S) state; and (iii) Debonded-Softening-Elastic-Softening-Debonded (D-S-E-S-D) state. Fig. 4 shows, in a synthesized way, these states during the debonding process of an overlapped bonded joint with a tubular cross-sectional area.

3.1. Elastic state (E)

Before any temperature variation is applied to the hybrid overlapped bonded joint, the full overlapped length is undeformed. However, once the temperature variations begin to increase, the entire overlapped length will be under the E state. In this first state, the interfacial slips within the entire overlapped length are lower than s_m and therefore, the

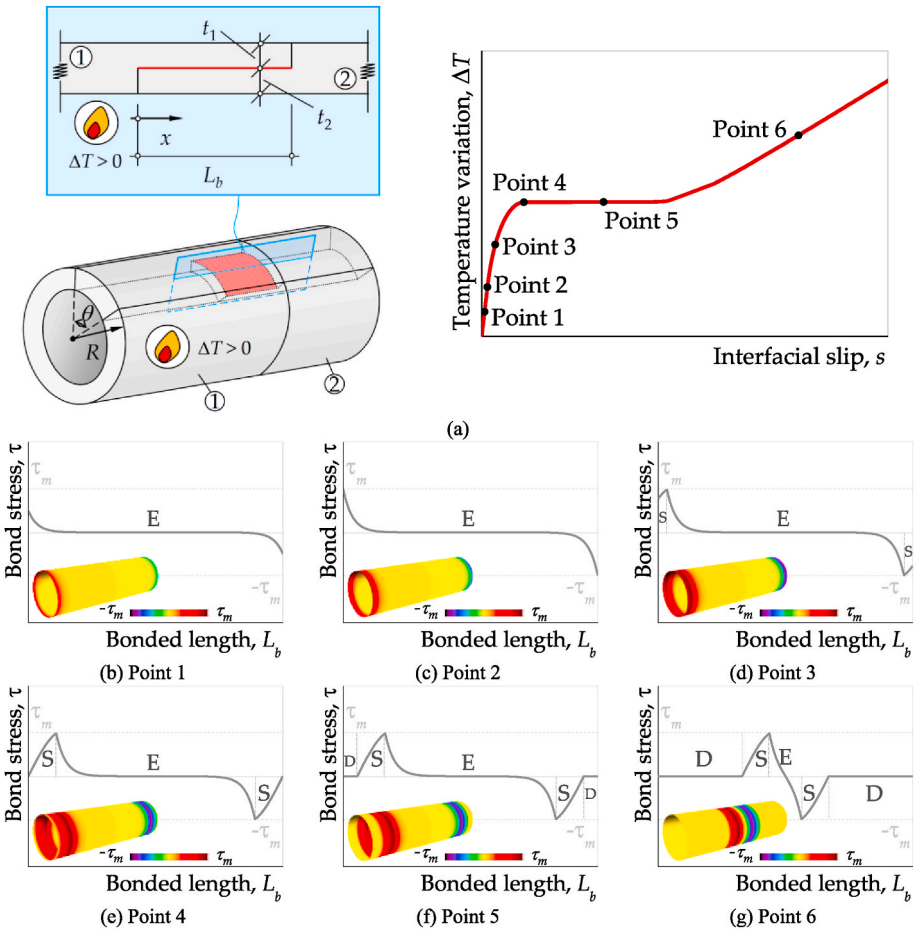

Fig. 4. Debonding process of an overlapped bonded joint with a tubular cross-sectional area subjected to thermal loading and without considering the T_g of the adhesive: (a) thermal loading *vs.* interfacial slip; (b) E state in which $\tau < \tau_m$; (c) limit of the E state in which $\tau = \tau_m$ at both ends of the joint; (d) S-E-S state; (e) end of the S-E-S state and initiation of the D-S-E-S-D state; (f) D-S-E-S-D state; and (g) somewhere in the D-S-E-S-D state at a higher thermal loading magnitude.

interfacial stresses are defined through the E stage of the bi-linear adhesive model according to:

$$\tau_E(s) = K_E \cdot s \tag{40}$$

where

$$K_E = \frac{\tau_m}{s_m}. \tag{41}$$

Thus, introducing Eq. (40) into Eq. (36), the hybrid overlapped bonded joint is governed by the following 2nd-order differential equation:

$$s_{,xx} - \gamma_e{}^2 \cdot s = 0 \tag{42}$$

where

$$\gamma_e{}^2 = K_E \cdot \lambda \tag{43}$$

To solve Eq. (42), since no loads are applied to material 1 at $x = 0$ nor in material 2 at $x = L_b$, the axial stresses in material 1 and material 2 obtained, respectively, from Eq. (27) and Eq. (30), have both a zero value. Thus, the solution of Eq. (42), i.e. the interfacial slip distribution of this E state is:

$$s_E(x) = \frac{(\alpha_1 - \alpha_2)\cdot\Delta T}{\gamma_e} \cdot \left[\sinh(\gamma_e \cdot x) + \frac{1 - \cosh(\gamma_e \cdot L_b)}{\sinh(\gamma_e \cdot L_b)} \cdot \cosh(\gamma_e \cdot x)\right] \tag{44}$$

based on Eq. (44), the interfacial stresses can be determined by simply introducing into it the equation that locally defines the elastic behaviour of the overlapped bonded joint stated in (40), i.e.:

$$\tau_E(x) = \frac{K_E \cdot (\alpha_1 - \alpha_2)\cdot\Delta T}{\gamma_e} \cdot \left[\sinh(\gamma_e \cdot x) + \frac{1 - \cosh(\gamma_e \cdot L_b)}{\sinh(\gamma_e \cdot L_b)} \cdot \cosh(\gamma_e \cdot x)\right] \tag{45}$$

If the first derivative of Eq. (44) with respect to x is introduced into Eq. (31), then the strains developed in material 1 are calculated according to:

$$u_{1,x}\big|_E = \frac{\Delta T}{1+r} \cdot \left[(\alpha_1 - \alpha_2) \cdot \left(\cosh(\gamma_e \cdot x) + \frac{1 - \cosh(\gamma_e \cdot L_b)}{\sinh(\gamma_e \cdot L_b)} \cdot \sinh(\gamma_e \cdot x)\right) + \alpha_2 + r \cdot \alpha_1\right] \tag{46}$$

whereas the same derivative of Eq. (44) with respect to x when introduced into Eq. (32) gives the expression of the strains developed in material 2 as follows

$$u_{2,x}\big|_E = \frac{\Delta T}{1+r} \cdot \left[- r \cdot (\alpha_1 - \alpha_2) \cdot \left(\cosh(\gamma_e \cdot x) + \frac{1 - \cosh(\gamma_e \cdot L_b)}{\sinh(\gamma_e \cdot L_b)} \cdot \sinh(\gamma_e \cdot x)\right) + \alpha_2 + r \cdot \alpha_1\right] \tag{47}$$

The end of this E state will be reached when both ends of the overlapped bonded joint, i.e. at $x = 0$ and at $x = L_b$, have the interfacial slip s_m. Therefore, considering that $s_E = s_m$ in Eq. (44), it will allow us to calculate the maximum temperature variation in the E state:

$$\Delta T = \frac{\gamma_e \cdot s_m}{\alpha_1 - \alpha_2} \cdot \frac{\sinh(\gamma_e \cdot L_b)}{1 - \cosh(\gamma_e \cdot L_b)} \tag{48}$$

However, in the presence of an infinite overlapped bonded length, the term with the hyperbolic functions tends to be one. Moreover, denoting $G_{F,E}$ as the elastic fracture energy of the adhesive model, i.e., the area limited by the elastic stage only, Eq. (48) can be rewritten as follows:

$$\Delta T_{\max,E} = \frac{2}{\alpha_1 - \alpha_2} \cdot \sqrt{\frac{G_{F,E} \cdot (R - t_1) \cdot (1 + r)}{(2R - t_1) \cdot E_1 t_1}} \tag{49}$$

where

$$G_{F,E} = \frac{\tau_m \cdot s_m}{2} \tag{50}$$

Another relevant aspect is the calculation of the overlapped bonded length that will be needed to consider ensuring that the E state will fully develop in it. Such needed overlapped bonded length should be sufficiently long enough that the maximum bond stress and its corresponding interfacial slip will be reached at both ends of the joint, i.e. at $x = 0$ and $x = L_b$. Therefore, it can be assumed that when $\gamma_e \bullet L_b = 4$, Eq. (48) will return the maximum value of ΔT, and consequently, the following expression can be written:

$$L_b = L_{b,E} = \frac{4}{\gamma_e} \tag{51}$$

Introducing Eq. (43) into Eq. (51) it leads to:

$$L_{b,E} = 2 \cdot \sqrt{\frac{2 \cdot (2R - t_1) \cdot E_1 t_1}{K_E \cdot (R - t_1) \cdot (1 + r)}} \tag{52}$$

3.2. Softening-Elastic-Softening state (S-E-S)

Once the interfacial slip s_m is reached in both ends of the overlapped bonded length, this new S-E-S state begins. Within the vicinities of both ends of the joint, the interfacial slips increase with the increase of the temperature, and the localization of s_m moves towards the centre of the overlapped joint. Therefore, the edges of the overlapped bonded joints are now softened whilst the centre is still within the E stage. The limited softened regions are equal on both edges of the joint and it is hereafter denoted as the softened length (L_S).

To solve the 2nd-order differential equation in (36), two other boundary conditions, beyond those already stated for the E state at $x = 0$ and $x = L_b$ (see the previous subsection), must be used. Therefore, at the left transition point between the S and the E stages, i.e. at $x = L_S$, a continuous strain field in material 1 should be ensured. Considering the symmetry of the problem, the other boundary condition is taken from the mid-point of the overlapped bonded joint where the interfacial slip is zero during the full debonding process of the joint. Using the two latter boundary conditions in Eq. (36), it is possible to obtain the interfacial slips of the E region:

$$s_E(x) = \frac{s_m \cdot \sinh\left[\gamma_e \cdot \left(\frac{L_b}{2} - x\right)\right]}{\sinh\left[\gamma_e \cdot \left(\frac{L_b}{2} - L_S\right)\right]} \tag{53}$$

where $L_S \le x \le L_b - L_S$, which corresponds to the centre of the overlapped bonded length of the joint between the S regions developed at both edges of the joint.

In the S regions, the interfacial slips are higher than s_m but lower than s_f and, for the S stage of the adhesive model, the interfacial stress is defined according to:

$$\tau_S(s) = K_S \cdot (s_f - s) \tag{54}$$

where

$$K_S = \frac{\tau_m}{s_f - s_m} \tag{55}$$

Introducing Eq. (54) into Eq. (36), the calculation of the interfacial slips within the S regions of the bonded joint is carried out by solving the following 2nd-order differential equation:

$$s_{,xx} + \gamma_s{}^2 \cdot (s - s_f) = 0 \tag{56}$$

where

$$\gamma_s{}^2 = K_S \cdot \lambda \tag{57}$$

To that end, using now the other two boundary conditions at $x = 0$ and $x = L_S$, the solution of Eq. (56) allows the calculation of the interfacial slips within the S regions of the overlapped bonded length as follows:

$$s_S(x) = s_f + \frac{\cos(\gamma_s \cdot x)}{\gamma_s \cdot \sin(\gamma_s \cdot L_S)} \cdot \left[(\alpha_1 - \alpha_2) \cdot \Delta T \cdot \cos(\gamma_s \cdot L_S) + \frac{\gamma_e \cdot s_m}{\tanh\left[\gamma_e \cdot \left(\frac{L_b}{2} - L_S\right)\right]} \right] + \frac{\sin(\gamma_s \cdot x)}{\gamma_s} \cdot (\alpha_1 - \alpha_2) \cdot \Delta T \tag{58}$$

where $0 \le x \le L_S$. However, it should be kept in mind that although Eq. (58) is used to define the left S region of the overlapped bonded length, the calculation of the interfacial slips developed at the other S region, i.e. on the right hand, can be made also with this same equation if instead of x it is used L_b - x.

To define the softened length L_S and know exactly where the S region ends and the E region begins, the following condition can be imposed on Eq. (58): at $x = L_S$, $s = s_m$. However, the term L_S cannot be isolated, and the temperature variation is isolated instead. Thus, the following equality is obtained.

$$\Delta T(L_S) = \frac{\gamma_s \cdot \sin(\gamma_s \cdot L_S) \cdot \tanh\left[\gamma_e \cdot \left(\frac{L_b}{2} - L_S\right)\right] \cdot (s_m - s_f) - \gamma_e \cdot s_m \cdot \cos(\gamma_s \cdot L_S)}{\tanh\left[\gamma_e \cdot \left(\frac{L_b}{2} - L_S\right)\right] \cdot (\alpha_1 - \alpha_2)} \tag{59}$$

It should be kept in mind that the value of ΔT to be obtained from Eq. (59) should be always higher than that obtained from Eq. (49), which has limited the maximum temperature variation in the E state. Also, the temperature variation is the parameter that is used to control the debonding process of the overlapped bonded joint. Thereby, when using (59) no explicit solution can be found for L_S unless a trial-and-error process is carried out after fixing a value for ΔT higher than that found in (49). By repeating this same process for several fixing ΔT, the relationship between ΔT and L_S can be plotted and the maximum value of ΔT allowed in the S-E-S state can be estimated.

Looking now at the determination of the interfacial stresses developed throughout the overlapped bonded length, these can be found by introducing Eq. (53) into Eq. (40) and by introducing Eq. (58) into Eq. (54), allowing, therefore, the calculation of the thermal expansion bond stresses within the E and S regions of the joint, respectively, according to:

$$\tau_E(x) = \frac{\tau_m \cdot \sinh\left[\gamma_e \cdot \left(\frac{L_b}{2} - x\right)\right]}{\sinh\left[\gamma_e \cdot \left(\frac{L_b}{2} - L_S\right)\right]} \tag{60}$$

and

$$\tau_S(x) = -K_S \cdot \left\{ \frac{\cos(\gamma_s \cdot x)}{\gamma_s \cdot \sin(\gamma_s \cdot L_S)} \cdot \left[(\alpha_1 - \alpha_2) \cdot \Delta T \cdot \cos(\gamma_s \cdot L_S) + \frac{\gamma_e \cdot s_m}{\tanh\left[\gamma_e \cdot \left(\frac{L_b}{2} - L_S\right)\right]} \right] + \frac{\sin(\gamma_s \cdot x)}{\gamma_s} \cdot (\alpha_1 - \alpha_2) \cdot \Delta T \right\} \tag{61}$$

The strains in material 1 and material 2 can be also determined. To that end, Eq. (31) and Eq. (32) can be used. So, the strains developed in material 1 within the E and S regions of the overlapped bonded joint are

obtained by introducing the first derivative of Eq. (53) with respect to x into Eq. (31) whilst the strains in material 1 within the S region are obtained by introducing the first derivative of Eq. (58) with respect to x into Eq. (31). Hence, the strain in material 1 within the E and S regions are defined, respectively:

$$u_{1,x}\big|_E = \frac{1}{1+r}\cdot\left[-\frac{\gamma_e\cdot s_m\cdot\cosh\left[\gamma_e\cdot\left(\frac{L_b}{2}-x\right)\right]}{\sinh\left[\gamma_e\cdot\left(\frac{L_b}{2}-L_S\right)\right]}+(r\cdot\alpha_1+\alpha_2)\cdot\Delta T\right] \tag{62}$$

and

$$u_{1,x}\big|_S = \frac{1}{1+r}\cdot\left\{-\frac{\sin(\gamma_s\cdot x)}{\sin(\gamma_s\cdot L_S)}\cdot\left[(\alpha_1-\alpha_2)\cdot\Delta T\cdot\cos(\gamma_s\cdot L_S)+\frac{\gamma_e\cdot s_m}{\tanh\left[\gamma_e\cdot\left(\frac{L_b}{2}-L_S\right)\right]}\right]\right.$$
$$\left.+[\cos(\gamma_s\cdot x)\cdot(\alpha_1-\alpha_2)+(r\cdot\alpha_1+\alpha_2)]\cdot\Delta T\right\} \tag{63}$$

Analogous to the determination of the strains developed in material 1, the strains in material 2 are determined by introducing the first derivatives of Eq. (53) and Eq. (58) with respect to x into Eq. (32). In the former case, the strains developed in the E region are determined as follows:

$$u_{2,x}\big|_E = \frac{1}{1+r}\cdot\left[\frac{r\cdot\gamma_e\cdot s_m\cdot\cosh\left[\gamma_e\cdot\left(\frac{L_b}{2}-x\right)\right]}{\sinh\left[\gamma_e\cdot\left(\frac{L_b}{2}-L_S\right)\right]}+(r\cdot\alpha_1+\alpha_2)\cdot\Delta T\right] \tag{64}$$

whilst the strains developed in the left-handed S region are:

$$u_{2,x}\big|_S = \frac{1}{1+r}\cdot\left\{\frac{r\cdot\sin(\gamma_s\cdot x)}{\sin(\gamma_s\cdot L_S)}\cdot\left[(\alpha_1-\alpha_2)\cdot\Delta T\cdot\cos(\gamma_s\cdot L_S)+\frac{\gamma_e\cdot s_m}{\tanh\left[\gamma_e\cdot\left(\frac{L_b}{2}-L_S\right)\right]}\right]\right.$$
$$\left.+[-r\cdot\cos(\gamma_s\cdot x)\cdot(\alpha_1-\alpha_2)+(r\cdot\alpha_1+\alpha_2)]\cdot\Delta T\right\} \tag{65}$$

The interfacial stresses or the strains in both materials developed at the right hand of the bonded joint, i.e. in the interval L_b - $L_S \le x \le L_b$, can be calculated if x in Eqs. (61), (63) and (65) are replaced by L_b - x.

3.3. Debonding-Softening-Elastic-Softening-debonding state (D-S-E-S-D)

The separation of material 1 from material 2 begins after the maximum temperature variation and the corresponding L_S is obtained from Eq. (59). At this exact moment, the interfacial slip at both edges of the overlapped bonded length has developed a slip equal to s_f on each edge and the softened length is maximized, i.e. $L_S = L_{S,\max}$. The increase of ΔT leads to the increase of the interfacial slip also and two debonded regions located at the right and left hand of the overlapped bonded joint tend to increase towards the centre of the joint. As these debonded lengths (L_D) increase, the E region tends to decrease while both S regions move towards the centre of the joint also. Due to the symmetric conditions of the debonding process, this stress transfer process will symmetrically develop with respect to the mid-point of the bonded length. Based on this symmetric condition, the analytical description of this D-S-E-S-D state can be carried out if Eq. (36) is applied to the E, S, and D regions of the overlapped bonded joint. Hence, with three different regions with three different stages, it is needed to use three different 2nd-order differential equations where the six following boundary conditions should be used: (i) at $x = L_b/2$, $s = 0$; (ii) at $x = L_S + L_D$, $s = s_m$; (iii) at $x = L_D$, $\sigma_1 = 0$; (iv) at $x = L_S + L_D$, the strains developed in material 1 are continuous; (v) at $x = L_D$, $s = s_f$, and (vi) at $x = 0$, $\sigma_1 = 0$.

For the definition of the E region, the 2nd-order differential equation stated in (42) can be used with the two first boundary conditions which lead to the interfacial slips:

$$s_E(x) = \frac{s_m\cdot\sinh\left[\gamma_e\cdot\left(\frac{L_b}{2}-x\right)\right]}{\sinh\left[\gamma_e\cdot\left(\frac{L_b}{2}-L_S-L_D\right)\right]} \tag{66}$$

Comparing Eq. (53) with Eq. (66), it can be noticed that both are the same if L_S in (53) is replaced by $L_S + L_D$.

To define the interfacial slip developed within the S region, the 2nd-order differential equation in (56) is used along with the third and fourth boundary conditions enumerated previously. Thus, the interfacial slips of the S regions are defined according to:

$$s_S(x) = -\frac{\gamma_e\cdot s_m\cdot\cos[\gamma_s\cdot(L_D-x)]}{\gamma_s\cdot\sin(\gamma_s\cdot L_S)\cdot\tanh\left[\gamma_e\cdot\left(L_D+L_S-\frac{L_b}{2}\right)\right]}+\frac{(\alpha_1-\alpha_2)\cdot\Delta T\cdot\cos[\gamma_s\cdot(L_S+L_D-x)]}{\gamma_s\cdot\sin(\gamma_s\cdot L_S)}+s_f \tag{67}$$

Finally, the interfacial slips of the D regions are obtained from:

$$s_{,xx} = {}^{xx}0 \tag{68}$$

which when integrated with the help of the fifth and sixth boundary conditions defined earlier, leads to the definition of the interfacial slips of the D regions, i.e.:

$$s_D(x) = (\alpha_1-\alpha_2)\cdot\Delta T\cdot(x-L_D)+s_f \tag{69}$$

To describe this state correctly, it is also needed to find the values of two distinct lengths for each temperature variation imposed on the joint. One corresponds to the softened length (L_S) and the other one to the debonded length (L_D). If in the case of the softened length its value tends to decrease with the increase of the temperature, the debonded length increases with the temperature. Hence, to calculate the values of L_S and L_D for a certain temperature variation, two independent equations are needed to define. These can be found by considering in Eq. (67) that $s = s_f$ at $x = L_D$, whereas the second equation can be obtained by assuming that $s = s_m$ at $x = L_S + L_D$ in Eq. (67) as well. Then, the following first and second equations will allow us to calculate, for a fixed temperature variation (which must be higher than that obtained from (59)), the corresponding values of L_S and L_D, i.e.:

$$\Delta T(L_S,L_D) = \left[(s_m-s_f)\cdot\gamma_s\cdot\sin(\gamma_s\cdot L_S)+\frac{\gamma_e\cdot s_m\cdot\cos(\gamma_s\cdot L_S)}{\tanh\left[\gamma_e\cdot\left(L_D+L_S-\frac{L_b}{2}\right)\right]}\right]\cdot\frac{1}{(\alpha_1-\alpha_2)} \tag{70}$$

and

$$\Delta T(L_S,L_D) = \frac{\gamma_e\cdot s_m}{\cos(\gamma_s\cdot L_S)\cdot\tanh\left[\gamma_e\cdot\left(L_D+L_S-\frac{L_b}{2}\right)\right]\cdot(\alpha_1-\alpha_2)} \tag{71}$$

Like in Eq. (59), these two equations (70) and (71) can only be solved numerically, and a new trial-and-error process should be implemented here. With these two lengths calculated, the interfacial slips in all the overlapped bonded length are defined. Thus, the interfacial stresses can be calculated if Eqs. (66) and (67) are introduced into Eq. (40) and Eq. (54), respectively. For the debonded regions, since material 1 has

already separated from material 2, the interfacial stresses in the debonded regions are always zero. Hence, the thermal expansion bond stresses in the elastic region located in the centre of the overlapped bonded length are:

$$\tau_E(x) = \frac{\tau_m \cdot \sinh\left[\gamma_e \cdot \left(\frac{L_b}{2} - x\right)\right]}{\sinh\left[\gamma_e \cdot \left(\frac{L_b}{2} - L_S - L_D\right)\right]} \tag{72}$$

whilst the thermal expansion bond stresses developed in the softened regions located between the E and D regions of the overlapped bonded length are defined according to:

$$\tau_S(x) = K_S \cdot \left\{ \frac{(\alpha_1 - \alpha_2)\cdot\Delta T \cdot \cos[\gamma_s \cdot (L_S + L_D - x)]}{\gamma_s \cdot \sin(\gamma_s \cdot L_S)} - \frac{\gamma_e \cdot s_m \cdot \cos[\gamma_s \cdot (L_D - x)]}{\gamma_s \cdot \sin(\gamma_s \cdot L_S) \cdot \tanh\left[\gamma_e \cdot \left(L_D + L_S - \frac{L_b}{2}\right)\right]} \right\} \tag{73}$$

Next, the strains developed in both materials are defined. To that end, Eq. (31) is used to define the strains in material 1 in the E, S, and D regions. Therefore, introducing the first derivatives of Eq. (66) and Eq. (67) with respect to x into Eq. (31), the strain in material 1 within the E and S regions are obtained, respectively, as follows:

$$u_{1,x}\big|_E = \frac{1}{1+r} \cdot \left[- \frac{\gamma_e \cdot s_m \cdot \cosh\left[\gamma_e \cdot \left(\frac{L_b}{2} - x\right)\right]}{\sinh\left[\gamma_e \cdot \left(\frac{L_b}{2} - L_S - L_D\right)\right]} + (r \cdot \alpha_1 + \alpha_2) \cdot \Delta T \right] \tag{74}$$

and

$$u_{1,x}\big|_S = \frac{1}{1+r} \cdot \left\{ - \frac{\gamma_e \cdot s_m \cdot \sin[\gamma_s \cdot (L_D - x)]}{\sin(\gamma_s \cdot L_S) \cdot \tanh\left[\gamma_e \cdot \left(L_D + L_S - \frac{L_b}{2}\right)\right]} + \left[\frac{(\alpha_1 - \alpha_2) \cdot \sin[\gamma_s \cdot (L_S + L_D - x)]}{\sin(\gamma_s \cdot L_S)} + (r \cdot \alpha_1 + \alpha_2) \right] \cdot \Delta T \right\} \tag{75}$$

Analogous, the strains developed in material 1 within the D region are determined from the first derivative of Eq. (69) with respect to x which when introduced into Eq. (31) leads to the following classical expression for the determination of the strains in a regular material subjected to a thermal loading:

$$u_{1,x}\big|_S = \alpha_1 \cdot \Delta T \tag{76}$$

The same reasoning applies to the definition of the strains developed in material 2, from which the strains in the E and S regions are, respectively:

$$u_{2,x}\big|_E = \frac{1}{1+r} \cdot \left[\frac{r \cdot \gamma_e \cdot s_m \cdot \cosh\left[\gamma_e \cdot \left(\frac{L_b}{2} - x\right)\right]}{\sinh\left[\gamma_e \cdot \left(\frac{L_b}{2} - L_S - L_D\right)\right]} + (r \cdot \alpha_1 + \alpha_2) \cdot \Delta T \right] \tag{77}$$

and

$$u_{2,x}\big|_S = \frac{1}{1+r} \cdot \left\{ \frac{r \cdot \gamma_e \cdot s_m \cdot \sin[\gamma_s \cdot (L_D - x)]}{\sin(\gamma_s \cdot L_S) \cdot \tanh\left[\gamma_e \cdot \left(L_D + L_S - \frac{L_b}{2}\right)\right]} + \left[(r \cdot \alpha_1 + \alpha_2) - \frac{r \cdot (\alpha_1 - \alpha_2) \cdot \sin[\gamma_s \cdot (L_S + L_D - x)]}{\sin(\gamma_s \cdot L_S)} \right] \cdot \Delta T \right\} \tag{78}$$

whereas in the D region, the strains developed in material 2 are:

$$u_{2,x}\big|_S = \alpha_2 \cdot \Delta T \tag{79}$$

Table 1
Main properties and geometries of the hybrid bonded joints under study.

No.	r (–)	R (mm)	E_1 (GPa)	t_2 (mm)	$E_1 \bullet A_1$ (kN/mm^2)	$E_2 \bullet A_2$ (kN/mm^2)	λ ($\times 10^{-6}$ mm^{-1})
1	0.2	15	61.7	2.5	125.8	194.0	13.215
2		30	66.7	2.5	257.7	429.6	12.548
3		45	68.3	2.5	389.7	665.2	12.354
4		60	69.1	2.5	521.6	900.8	12.262
5		15	110.9	5	125.8	348.7	7.351
6		30	127.3	5	257.7	820.0	6.575
7		45	132.5	5	389.7	1291.2	6.365
8		60	135.2	5	521.6	1762.4	6.267
9		15	147.6	7.5	125.8	464.2	5.523
10		30	181.7	7.5	257.7	1171.0	4.604
11		45	192.8	7.5	389.7	1877.9	4.376
12		60	198.2	7.5	521.6	2584.7	4.273
13		15	171.8	10	125.8	540.3	4.744
14		30	230.1	10	257.7	1482.8	3.636
15		45	249.0	10	389.7	2425.3	3.389
16		60	258.3	10	521.6	3367.8	3.280
17	0.8	15	246.8	2.5	125.8	194.0	4.956
18		30	266.7	2.5	257.7	429.6	4.706
19		45	273.1	2.5	389.7	665.2	4.633
20		60	276.3	2.5	521.6	900.8	4.598
21		15	443.6	5	125.8	348.7	2.757
22		30	509.0	5	257.7	820.0	2.466
23		45	530.2	5	389.7	1291.2	2.387
24		60	540.6	5	521.6	1762.4	2.350
25		15	590.4	7.5	125.8	464.2	2.071
26		30	727.0	7.5	257.7	1171.0	1.726
27		45	771.0	7.5	389.7	1877.9	1.641
28		60	792.8	7.5	521.6	2584.7	1.603
29		15	687.3	10	125.8	540.3	1.779
30		30	920.5	10	257.7	1482.8	1.363
31		45	995.8	10	389.7	2425.3	1.271
32		60	1033.0	10	521.6	3367.8	1.230
33	1	15	308.4	2.5	125.8	194.0	4.405
34		30	333.3	2.5	257.7	429.6	4.183
35		45	341.4	2.5	389.7	665.2	4.118
36		60	345.4	2.5	521.6	900.8	4.087
37		15	554.4	5	125.8	348.7	2.450
38		30	636.3	5	257.7	820.0	2.192
39		45	662.7	5	389.7	1291.2	2.122
40		60	675.7	5	521.6	1762.4	2.089
41		15	738.0	7.5	125.8	464.2	1.841
42		30	908.7	7.5	257.7	1171.0	1.534
43		45	963.8	7.5	389.7	1877.9	1.459
44		60	991.0	7.5	521.6	2584.7	1.424
45		15	859.1	10	125.8	540.3	1.581
46		30	1150.7	10	257.7	1482.8	1.212
47		45	1244.8	10	389.7	2425.3	1.130
48		60	1291.3	10	521.6	3367.8	1.093

4. Numerical validation

To validate the proposed analytical model, several hybrid bonded joints with different properties and geometries are analysed through the Finite Element Method (FEM). The numerical models were carried out with the commercial software package LS-DYNA R12 (Hallquist, 2006). A total of 48 three-dimensional models were considered with the properties and geometries defined in Table 1. The main goal of these numerous numerical simulations is to cover a wide range of situations that can, therefore, validate the proposed analytical model. Thereby, the following four parameters were considered in the numerical models: (i) the axial stiffness r as defined in Eq. (29); (ii) the elastic modulus of the adherends 1 (E_1); (iii) the thickness of the adherend 2 (t_2); and (iv) the external radius of curvature (R). To represent a steel substrate, the elastic modulus of the adherend 2 was set equal to $E_2 = 200$ GPa whilst the thickness of the adherend 1 was $t_1 = 1.4$ mm which is a common thickness found in CFRP laminates (Biscaia and Diogo, 2020). It should be bear in mind also that since the angle θ is supposed to not influence the temperature capacity of the bonded joints nor the strains or thermal

bond stresses, the numerical simulations were carried out by assuming circular and/or tubular bonded joints (i.e. $\theta = 360°$).

During the subsequent analyses, some simplifications were adopted to prevent the increase of the text unnecessarily and make more fluent the readability of the text. Therefore, three axial stiffness ratios were selected, which ensures that the model may cover a low ($r = 0.2$), a high ($r = 0.8$), or an axial stiffness ratio value equal to one. In addition, the implemented CZM in all the numerical simulations was always the same. The thickness of the element to model the crack opening between the outer material (herein defined as material 1) and the inner material (i.e. material 2) is nil. The CZM is based on a bilinear bond-slip relationship like the one represented in Fig. 1. At room temperature, with no temperature variations, the parameters needed to define the bond-slip relationship are $s_m = 0.106$ mm, $\tau_m = 19.65$ MPa (i.e. with an elastic stiffness of $K_E = 185.4$ MPa/mm and elastic fracture energy of $G_{F,E} = 1.041$ N/mm), $s_f = 0.220$ mm (i.e. with a softening stiffness of $K_S = 172.37$ MPa/mm) and $G_F = 2.162$ N/mm. With these values, the local bond-slip relationship is suitable for applying to CFRP-to-steel bonded joints as mentioned in the literature (Biscaia and Ribeiro, 2019). Another simplicity herein considered is the overlapped bonded length of the joints that was kept the same in all the numerical simulations (i.e. $L_b = 350$ mm). Finally, and to be consistent with a CFRP-to-steel bonded joint, the thermal expansion coefficient of the outer material is $\alpha_1 = 0.3 \times 10^{-6}/°C$ whilst, for the inner material thermal it was adopted a thermal expansion coefficient of $\alpha_2 = 12 \times 10^{-6}/°C$ (Biscaia and Ribeiro, 2019). With these thermal expansion coefficients, the outer material will be the CFRP composite whereas the inner material will be the steel.

4.1. The finite element model

To model several three-dimensional real problems with a high level of accuracy, LS-DYNA R12 (Hallquist, 2006) has been used in a wide range of applications, such as in the automobile, aerospace, construction, military, manufacturing, or bioengineering industries (Tho et al., 2004; Xiao et al., 2009; Wenk et al., 2009; Filice et al., 2010; Hussain et al., 2013; Ahmeda et al., 2014; Rawat and Singh, 2017; Salvado et al., 2017; Bolisetti et al., 2018; Carvalho et al., 2018; Li et al., 2019; Luo et al., 2019; Kumar and Shrivaathsav, 2019). In the present work, 3D models of the tubular hybrid bonded joints were developed. A regular mesh of 8-noded hexahedrons with a fully integrated element formulation was adopted in the 48 different cases listed in Table 1. To avoid losing the efficiency of the numerical simulations, the development of their geometries was based on the three following main criteria: (i) use of three finite elements along with the thickness of each cylinder or tube with the same thickness; (ii) as already shown in some experimental works available in the literature (Biscaia, 2019, 2020; Biscaia et al., 2015b; Maazoun et al., 2019; Alhassan et al., 2020), the adopted size of the finite elements is 1 mm along the overlapped bonded length; and (iii) use of 24 elements along the perimeter of the tubular cross-section when $R = 15$ mm, 48 elements when $R = 30$ mm, 72 elements when $R = 45$ mm (see Fig. 5) and 96 elements when $R = 60$ mm.

To simulate the thermal loading condition and promote the debonding process previously described in Section 3, a monotonic temperature variation was applied to the adherends. This increase in the thermal loading led the numerical specimens to their interfacial failure,

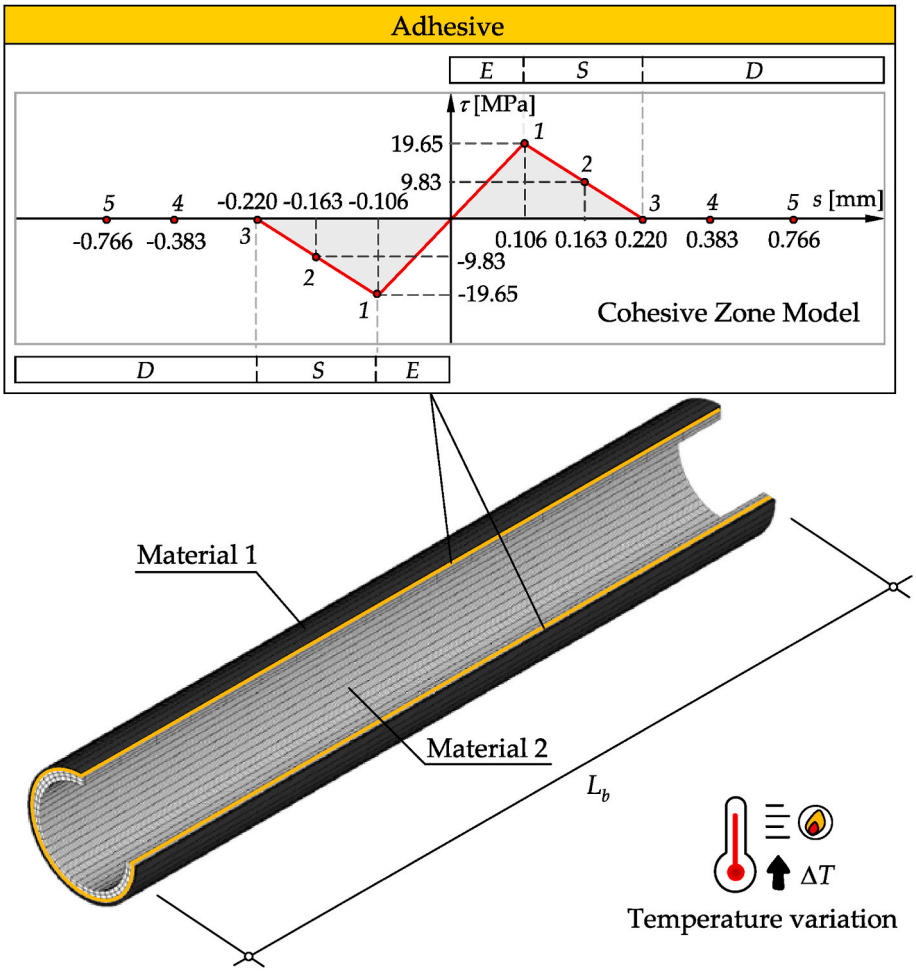

Fig. 5. Overview of the generated mesh of the 3D numerical models with a tubular cross-sectional area developed in LS-DYNA R12 (Hallquist, 2006) in which $R = 30$ mm and $t_2 = 5.0$ mm.

being the numerical solutions computed using a non-linear implicit solver, for which the maximum increment was limited to 0.1% of the total temperature variation applied to the model. The results acquired from the numerical simulations were the thermal expansion bond stresses and the interfacial slips of the cohesive elements throughout the interface along the path spaced by 1 mm between them. The strains developed in the adherents were obtained also.

4.2. The thermal loading vs. interfacial slip relationships

The accuracy of the proposed model to estimate the thermal loading *vs.* interfacial slip relationships of all hybrid bonded joints in Table 1 can be seen from Figs. 6–8. These three figures are grouped according to the axial stiffness ratio adopted for the bonded joints. In the case of the temperature-slip curves shown in Fig. 6, the results correspond to the bonded joints with $r = 0.2$ mm whilst Figs. 7 and 8 show the curves obtained from the joints with $r = 0.8$ and $r = 1.0$ mm, respectively.

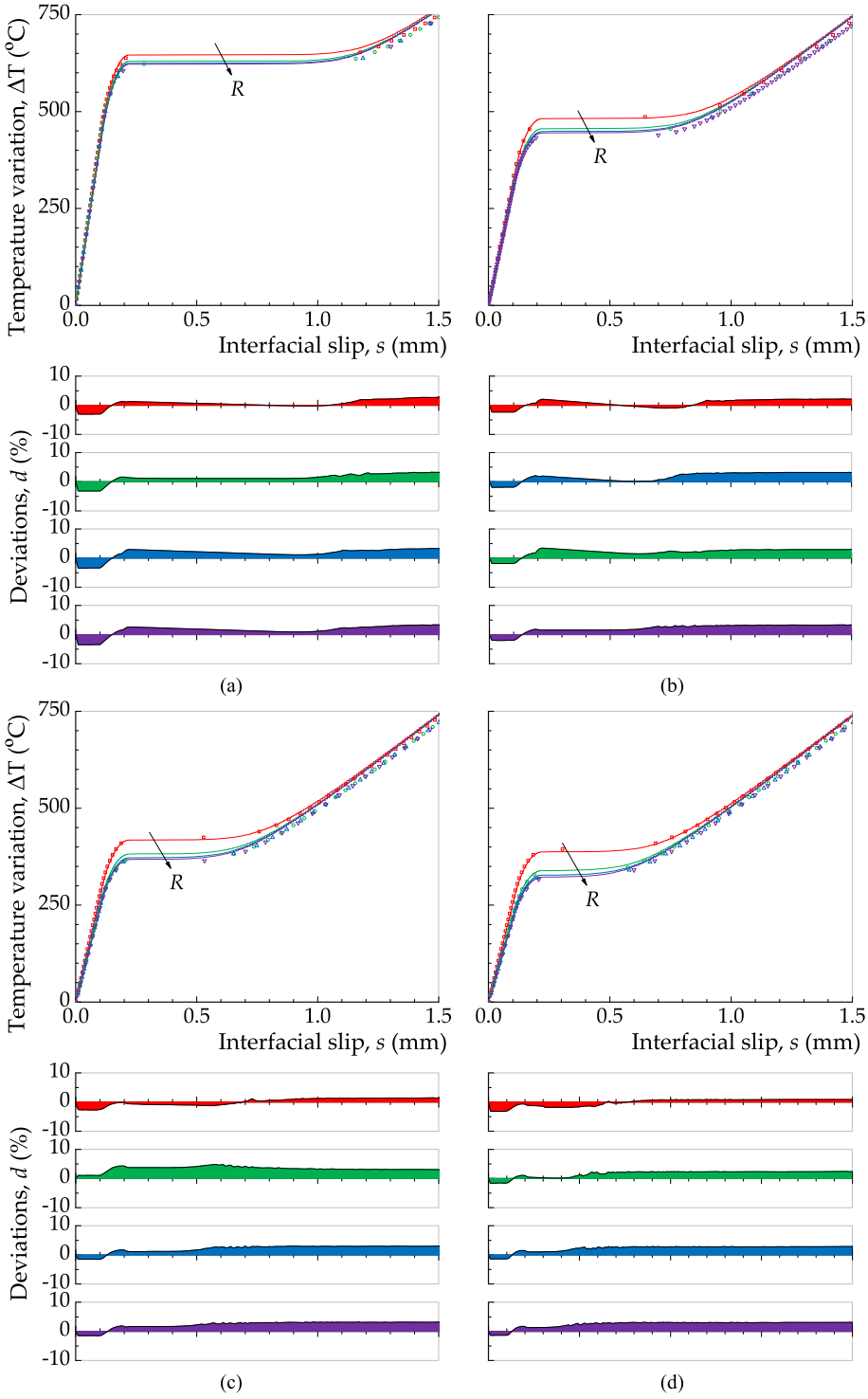

Fig. 6. Comparison between the thermal loading *vs.* interfacial slip relationships obtained from the analytical model with that obtained from the LS-DYNA R12 (Hallquist, 2006) when $r = 0.2$ and: (a) $t_2 = 2.5$ mm; (b) $t_2 = 5.0$ mm; (c) $t_2 = 7.5$ mm; and (d) $t_2 = 10.0$ mm.

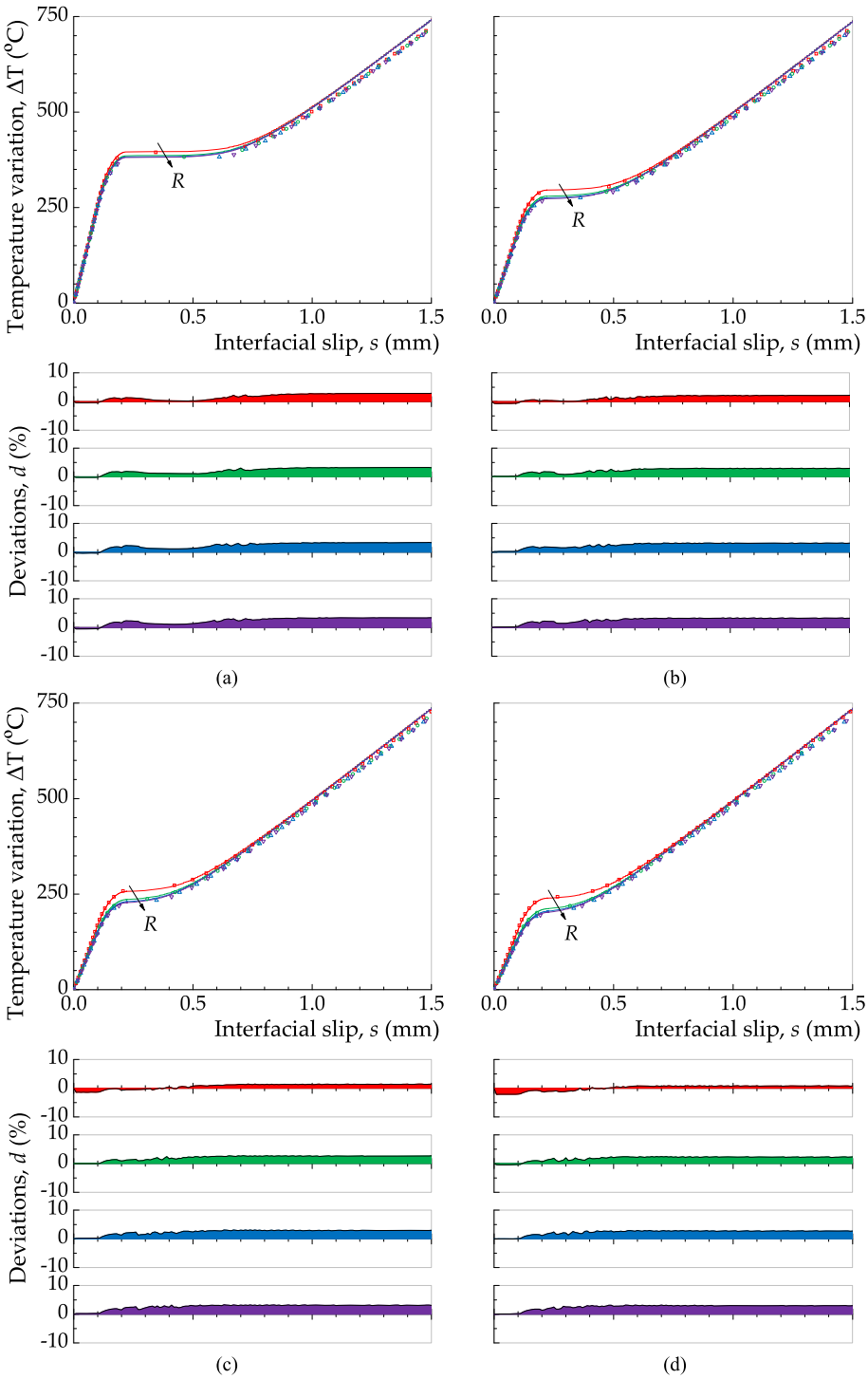

Fig. 7. Comparison between the thermal loading *vs.* interfacial slip relationships obtained from the analytical model with that obtained from the LS-DYNA R12 (Hallquist, 2006) when $r = 0.8$ and: (a) $t_2 = 2.5$ mm; (b) $t_2 = 5.0$ mm; (c) $t_2 = 7.5$ mm; and (d) $t_2 = 10.0$ mm.

Based on the thermal loading *vs.* interfacial slip relationships, the relative deviations (d) between the analytical results and the numerical ones were determined along with the debonding processes of each joint. Thus, the values of d shown in Figs. 6–8 were calculated as follows:

$$d(\%) = \frac{v_{a,i} - v_{n,i}}{v_{n,i}} \tag{80}$$

where $v_{a,i}$ and $v_{n,i}$ are the values obtained from the analytical and numerical methods, respectively, at the same fixed interfacial slip i.

The results herein reported in Figs. 6–8 allow us to asseverate that the proposed analytical model tracks the numerical simulations very closely during the full debonding processes of the different bonded joints under study. In none of the 48 studied cases, the deviation of the analytical model from the numerical one exceeded an absolute value of 5% which attests, despite its simplicity, to the very good accuracy of the proposed analytical model. In all the simulated joints, the temperature-slip curves obtained from the numerical method confirmed the analytical predictions. Thus, the temperature-slip response of hybrid bonded joints when subjected to a temperature variation is characterized by an initial linear increase which is followed by a nonlinear one. After that, a

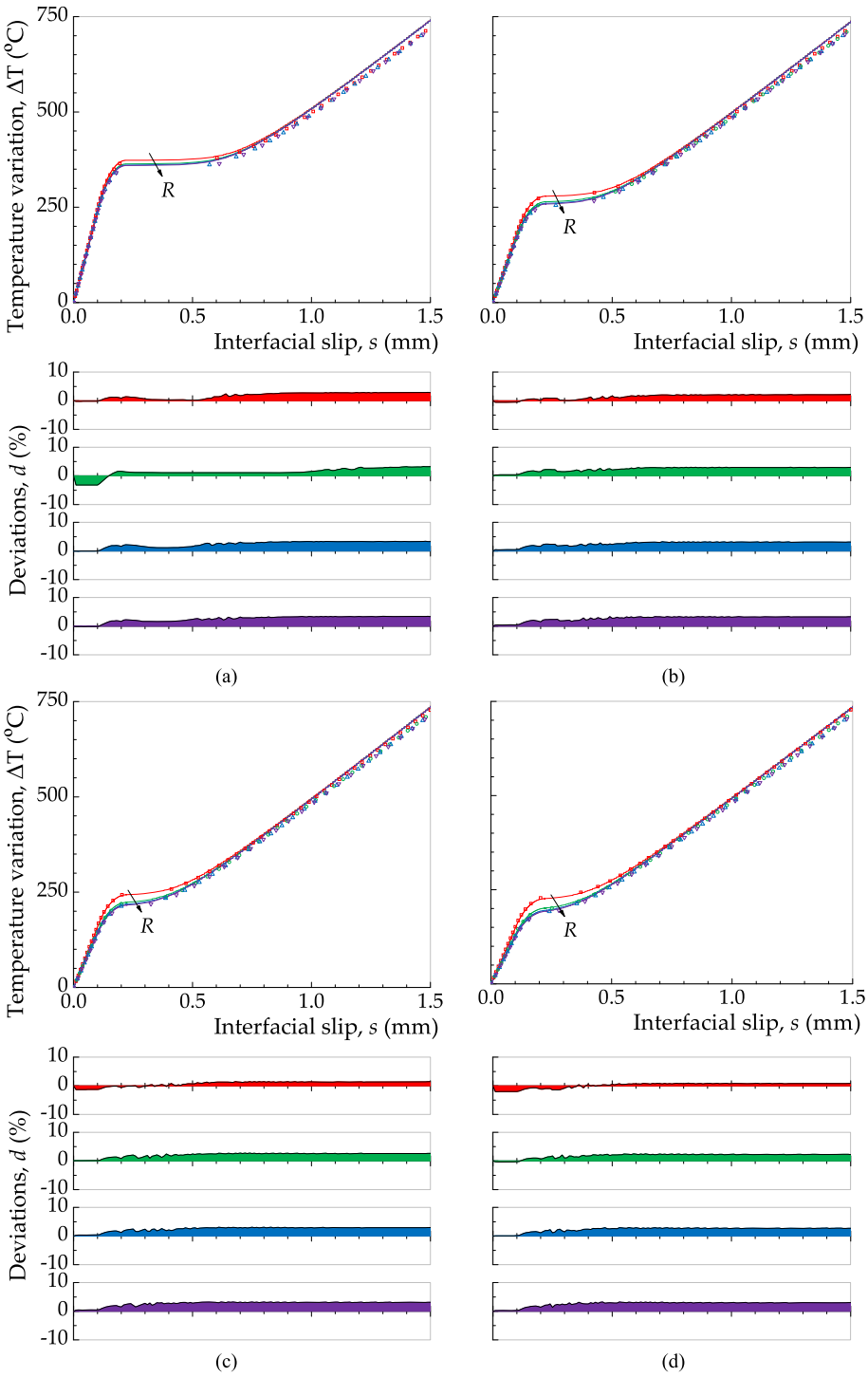

Fig. 8. Comparison between the thermal loading *vs.* interfacial slip relationships obtained from the analytical model with that obtained from the LS-DYNA R12 (Hallquist, 2006) when $r = 1.0$ and: (a) $t_2 = 2.5$ mm; (b) $t_2 = 5.0$ mm; (c) $t_2 = 7.5$ mm; and (d) $t_2 = 10.0$ mm.

plateau is obtained, and its end is followed by another increase in the temperature with the interfacial slip. Although this transition between this plateau and the final linear stage is carried out in a nonlinear way, the temperature-slip relationship at higher temperature variation (or interfacial slip) magnitudes tends to be linear as defined in Eq. (69).

Based on both results, analytical and numerical, it can be noticed that the increase in the radius of the hybrid bonded joint decreases the maximum temperature beyond which the debonding takes place. Nevertheless, for the highest radii, the decrease of that maximum temperature loses its relevance in the debonding process since, for the same interfacial slip, the temperature decrease is almost marginal between the hybrid bonded joints with $R = 45$ mm and $R = 60$ mm. It can be also found that by increasing the axial stiffness ratio of the bonded joint, the temperature beyond which the complete separation between materials takes place decreases. In fact, at this moment, the separation between materials propagates from both ends towards the centre of the hybrid bonded joint. As the overlapped bonded joint increases, the previously mentioned plateau in the temperature-slip curves tends to increase as well.

Another interesting aspect revealed by these models lies in the

influence of the axial stiffness ratio and the external radius curvature on the plateau observed in the temperature-slip response of all joints. Hence, as the external radius curvature or the axial stiffness ratio increase, that plateau tends to decrease. This reveals that the effective bond length, i.e. the length beyond which the maximum temperature to completely separate the adherends can be reached, tends to decrease. In other words, and remembering that the same overlapped bonded length of 350 mm was adopted in all the models, as the length of the plateau observed in the temperature-slip curves decreases, the effective bond length of the hybrid bonded joint increases.

4.3. The interfacial slip and thermal expansion bond stress configurations

The amount of generated data prevents us to show all the slip and bond stress distributions obtained from all the models and, for this motive, the following analyses are focused on the tenth studied model (see Table 1), in which the mechanical properties of the adherends are more adequate to represent a hybrid bonded joint between a CFRP composite with a normal elastic modulus and a steel substrate (Ghafoori and Motavalli, 2015; Yang et al., 2018). Therefore, the accuracy of the analytical proposed model to estimate the slip and the bond stress distributions throughout the overlapped bonded length is investigated.

Furthermore, to facilitate the readability of the figures, and from here after, the comparisons of the results obtained from the analytical proposed model with the numerical simulations are based on five fixed interfacial slips (see Fig. 5): (i) with $s = s_m = 0.106$ mm which aims to show, although in its limit, the E stage of the interface; (ii) with $s = 0.163$ mm which correponds the average slip of the S stage of the bond-slip relationship and it aims to show a point within the S-E-S state of the joint; (iii) with $s = s_f = 0.220$ mm which aims to show the initiation of the separation between adherends, i.e. when the S-E-S stage ends and the D-S-E-S-D state begins; (iv) with $s = 0.363$ mm which is 65% more than s_f and it aims to show an earlier debonding state (D-S-E-S-D) of the interface where both ends of the adherends developed no bond stresses; and (v) with $s = 0.766$ mm, which corresponds to approximately 3.5 times the value of s_f and it aims to show an advanced debonding state (D-S-E-S-D) of the joint.

Fig. 9a shows the interfacial slip configurations obtained by both methods, analytical and numerical, at the five nominated interfacial slips. Both results show that the highest interfacial slips develop at both ends of the joint with the increase in temperature. On the contrary, the models predict no interfacial slips at the midpoint of the joint during the

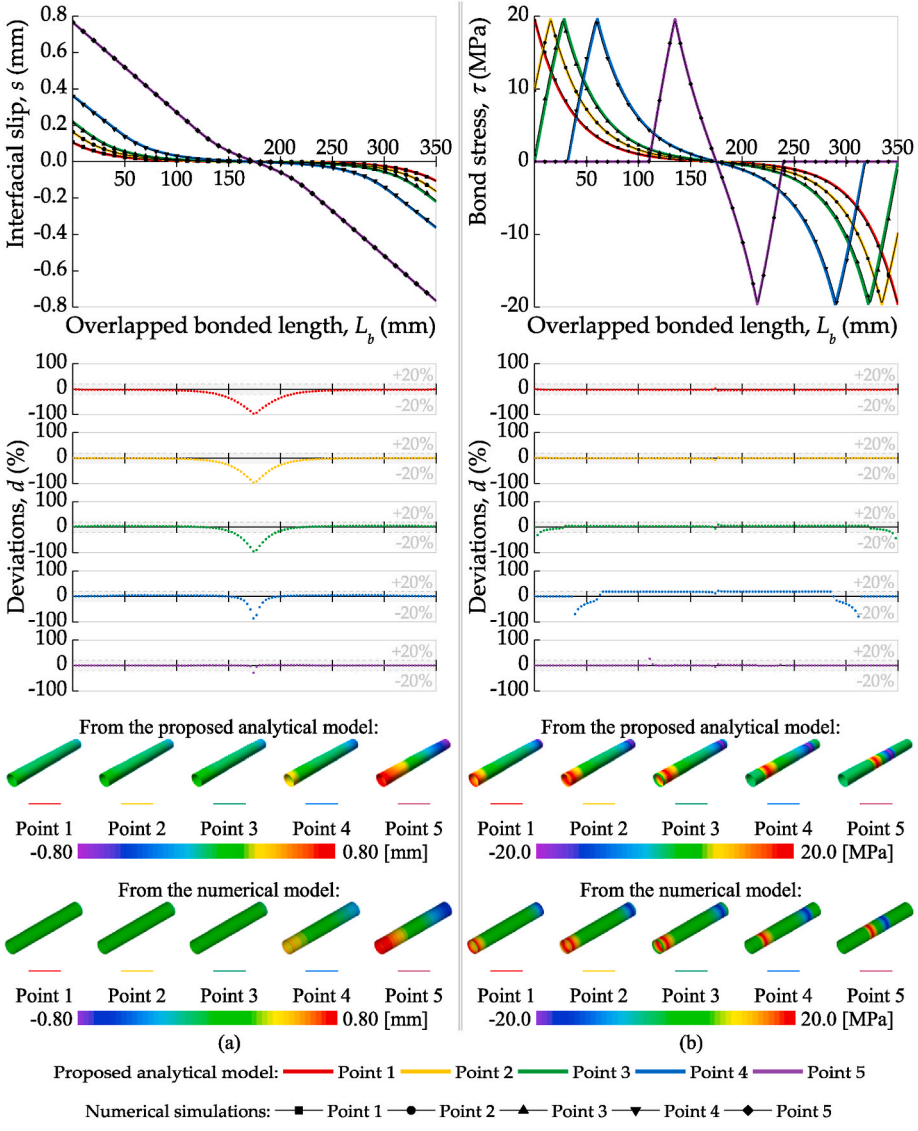

Fig. 9. Comparison between the analytical proposed model with the numerical simulations of the tenth studied case: (a) interfacial slip distributions; and (b) bond stress distributions.

debonding process. Although the debonding problem is under symmetry conditions, the interfacial slip configurations have anti-symmetric developments to the mid-point of the overlapped bonded length. Along with the interfacial slip configurations, the relative deviations (d) of the analytical model from the numerical simulations were also calculated. In general, the calculated deviations are lower than an absolute value of 20% but in the vicinity of the centre of the joint where the interfacial slips have quite low values, the deviations of the analytical data from the numerical ones deviate almost 100%. Of course, such high deviations are closely related to the very small interfacial slips developed at the centre of the bonded joint.

Based on these interfacial slips, the thermal expansion bond stresses can be determined by using the bond-slip relationship of the joint. For instance, all the slips lower than 0.106 mm led to thermal expansion bond stress values lower than 19.65 MPa (see Fig. 5). In this condition, the configuration of the thermal expansion bond stresses decreases in a nonlinear way from 19.65 MPa until 0 MPa at the centre of the joint. With slip values between 0.106 mm and 0.220 mm the thermal expansion bond stress also decreases nonlinearly from 19.65 MPa to 0 MPa. The main difference between these two conditions lies in the fact that the 0 MPa at the mid-point of the overlapped bonded joint will never change whereas the 0 MPa of the second situation will tend to move towards the centre of the joint as the complete separation between adherends develops. Like the slip configurations, the bond stresses also have an anti-symmetric configuration to the mid-point of the overlapped bonded joint as Fig. 9b reveals. In terms of the deviations, the results obtained from the analytical model tended to overestimate the numerical results. In general, and considering the five nominated slips at the CFRP both ends, the analytical results never exceeded an absolute value of 20% from the numerical ones, which attests to the good accuracy of the former method.

4.4. Configurations of the strains developed in the adherents

The strains developed in the adherends (CFRP and steel) are shown in Fig. 10. In the case of the strains developed in material 1 (i.e. in the CFRP composite), the results reported in Fig. 10a clearly show that the highest strains developing at the centre of the overlapped bonded length tend to decrease nonlinearly towards the CFRP both ends. The highest CFRP strain values were obtained when the complete separation from the steel is initiated (i.e. at the third nominated slip). From this point afterwards, the CFRP strains tend to decrease. Looking at the calculated deviations, it can be noticed that, once again, the absolute value of 20% was marginally exceeded. Still, some deviations outside the interval

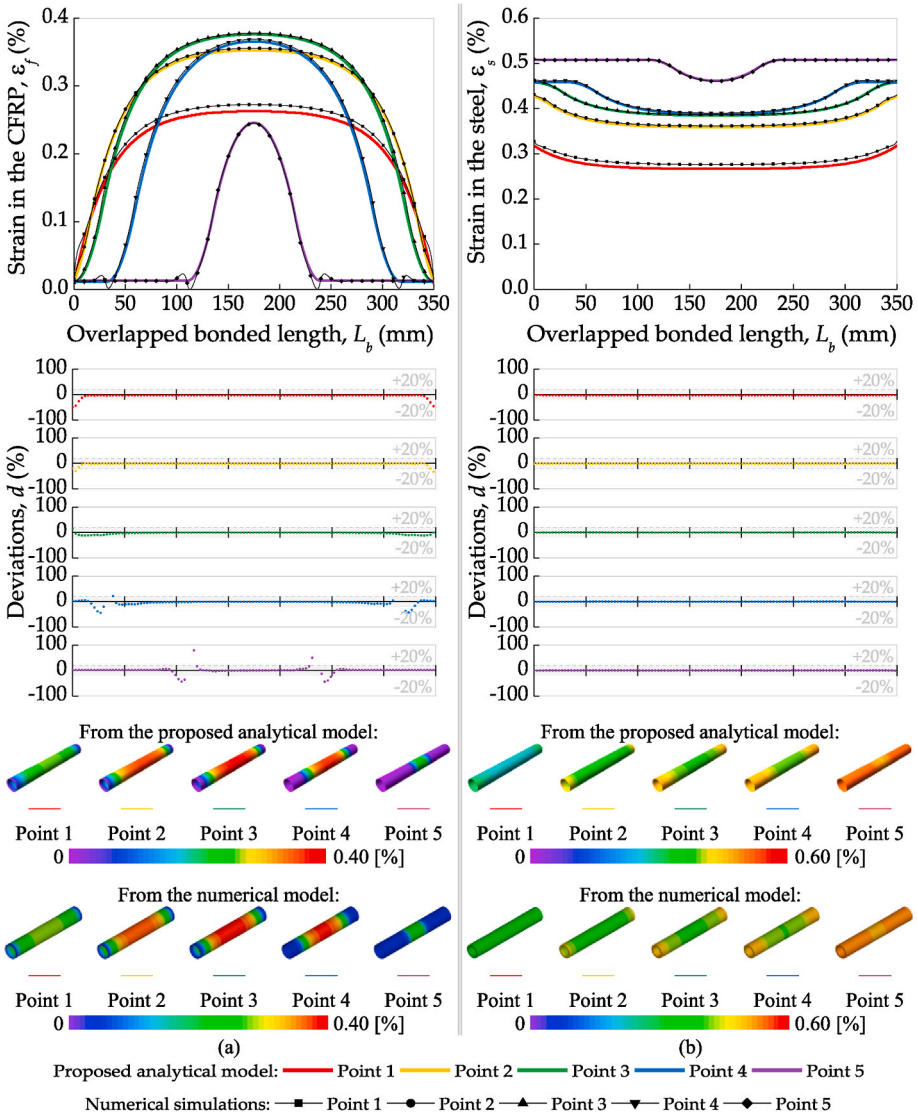

Fig. 10. Comparison between the analytical proposed model with the numerical simulations of the tenth studied case: (a) configurations of the strains developed in the CFRP composite (i.e. material 1); and (b) configurations of the strains developed in the steel (i.e. material 2).

between −20% and 20% were determined mainly at both ends of the CFRP composite where the values of the developed strains are quite low. It should be noticed also that at the last two nominated interfacial slips (at Points 4 and 5), the numerical simulations showed some small fluctuations at the transition points between the debonded and softened regions. Since the analytical method did not capture this perturbation, such fluctuations were attributed to a numerical issue that had low significance on the estimation of the strains developed in the CFRP composite.

On the other hand, the strains developed in the steel (i.e. material 2) are shown in Fig. 10b. The configuration of the strains in the steel is completely different from that obtained from the CFRP composite. So, unlike the strains developed in the CFRP composite, the maximum strains developed in the steel are localized at both ends of the joint and tend to decrease towards the mid-point of the overlapped bonded joint where it reaches its minimum strain value. Furthermore, the strains in the steel tend to increase despite the complete separation between adherends has been initiated. Along with the complete separation between materials, the debonded regions led the strains in the steel into a constant development that drops to lower values in the centre region of the joint where the adherends have not completely separated yet. In this case, the calculated deviations for the five nominated slips throughout the overlapped bonded length had marginal values. The highest deviations were calculated for the first nominated interfacial slip in which the deviations of the analytical model did not exceed the absolute value of 4% from the numerical simulations.

5. Influence of T_g on the debonding process

The influence of T_g on the debonding process has been ignored so far. Nevertheless, it allowed us to show all the states that the hybrid bonded joints undergo until their complete interfacial debonding failure. As already explained before, T_g is an important parameter with a high impact on the final bond performance of hybrid joints. Therefore, this section is dedicated to showing how the proposed analytical model estimates the debonding process of a hybrid bonded joint with a tubular cross-sectional area when the T_g of the adhesive is considered. Once again, to avoid increasing the text unnecessarily, the tenth example in Table 1 is presented and it has the intention to simulate a CFRP-to-steel bonded joint in which the CFRP composite is material 1 whereas the steel substrate is material 2.

The influence of the temperature variations on the local bond-slip relationship is simulated through the model briefly described in subsection 2.2. To compare both methods, analytical and numerical, the already mentioned temperature-dependent bond-slip model was also implemented into the LS-DYNA R12 software (Hallquist, 2006). Furthermore, considering that the bonding between a CFRP composite onto a steel substrate is usually performed with epoxy resins, the T_g value assumed for the epoxy resin is 62 °C, which is the same value obtained for the epoxy resin used by Klamer (2006). It should be kept in mind that if the joining of the CFRP composite onto the steel substrate is carried out at 25 °C, a temperature variation of only 37 °C will be needed to reach the T_g of the adhesive. This shows how problematic the thermal loading may be for the integrity of the hybrid bonded joints.

Fig. 11 shows the relationship between the thermal loading and the interfacial slip of the CFRP-to-steel bonded joint (i.e. tenth example in Table 1) with the influence of T_g. Although already shown in Fig. 6c, the same relationship without considering the influence of T_g is presented for comparisons purposes. As can be seen from Fig. 11, when the T_g is considered in the debonding process of the CFRP-to-steel joint, the interfacial failure is reached for a low-temperature variation. The proposed analytical method agreed very well with the numerical simulations with deviations that never outfitted the interval from −4% to 4%.

The prediction of the interfacial failure of the CFRP-to-steel bonded joint was considered when the maximum bond stress reached a value lower than 1% of its corresponding situation with no temperature variation (i.e. 19.65 MPa). Under this assumption, the temperature variation beyond which the CFRP-to-steel bonded joint would have failed would be 77.5 °C whilst the numerical simulations predicted the failure of the joint at a temperature variation of 77.0 °C, which is less than 1% deviation from that predicted on the analytical proposed model. At this temperature variation of 77.0 °C, the influence of T_g lead to an interfacial slip increase in both methods of almost 420%.

From Fig. 12, it can be noticed how the T_g has influenced the interfacial stress transfer between the CFRP composite and the steel. Since the interfacial debonding of the CFRP-to-steel joint was reached before the second nominated point, only the bond stresses corresponding to the first nominated slip are shown. At this first nominated slip (i.e. for 0.106 mm) the temperature variation obtained from the analytical method has reached 67.0 °C and the maximum bond stress that is expected to be developed within the CFRP-to-steel interface is 0.70 MPa, which is a reduction of 96.4% from its maximum and initial value. At this temperature variation, the analytical results track very closely the numerical ones once again which shows the versatility of the proposed analytical model in predicting the debonding process of a tubular hybrid bonded joint whether the T_g is or is not considered.

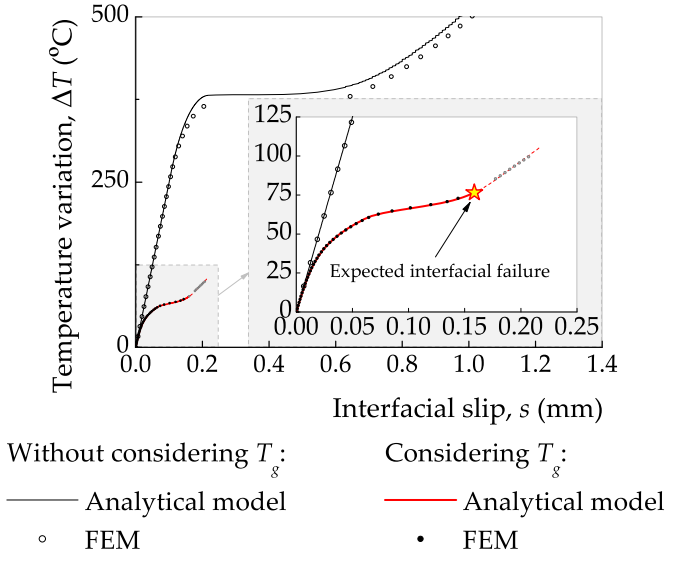

Fig. 11. Influence of T_g on the thermal loading *vs.* interfacial relationship.

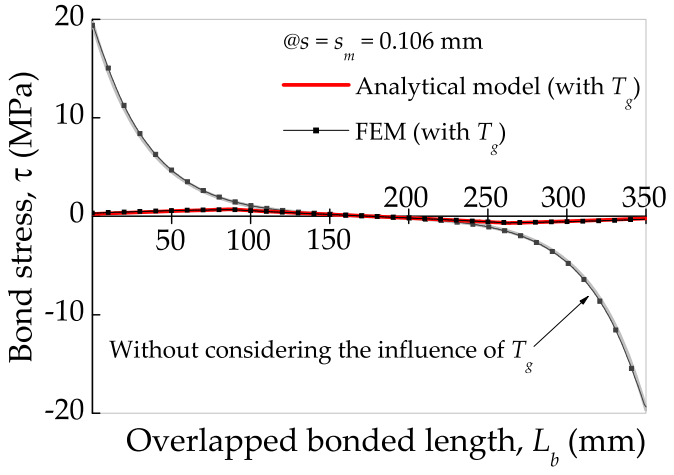

Fig. 12. Thermal expansion bond stresses developed within the CFRP-to-steel joint with and without the influence of T_g.

6. Conclusions

The debonding process of circular or tubular hybrid bonded joints was analytically described and confirmed by a three-dimensional software based on the FEM. To validate the proposed analytical model, several cases with different parameters were analysed. The importance of T_g for the debonding process of the bonded joints subjected to temperature variations was also presented and discussed. Therefore, and based on the results obtained in this work, the following main conclusions can be drawn:

- until its interfacial failure, a circular or tubular hybrid bonded joint undergoes through three states: E, S-E-S, and D-S-E-S-D. In all these, the interfacial slip and thermal expansion bond stress configurations have an anti-symmetry development to the mid-point of the joint. However, the configuration of the strains in the adherends is symmetric to the centre of the joint;
- despite its simplicity and when confronted with the three-dimensional FE analyses, the proposed analytical method was able to reproduce the debonding failure of the tubular hybrid bonded joint with very good accuracy. In fact, in all of the studied situations, the calculated deviations rarely exceeded an absolute deviation of 5% from the numerical simulations;
- both methods showed that the increase of temperature has a distinct impact on the strains developed in both adherends. If in the outer adherend the maximum strains are localized at the centre of the bonded joint, in the inner adherend the maximum strains are localized at both edges of the joint. Therefore, and for a different failure mode beyond the interfacial one, it is expected that the outer adherend may collapse at the centre of the joint, whilst the results suggest that the rupture of the inner adherend will occur at the edges of the joint;
- the axial stiffness of the joint (r) has an influence also on the temperature beyond which the adherends begin to physically separate between them. So, as the axial stiffness increases, this temperature tends to decrease which means that hybrid bonded joints with low r values can stand for higher temperature variations. However, the increase of the external circular curvature (R) of the joint also tends to decrease, although not very much, this maximum temperature. Nevertheless, the results showed that for a certain value of R the decrease of this temperature also tends to a steady condition;
- the influence of T_g on the integrity of the tubular (or circular) hybrid bonded joint is crucial for their serviceability state. In the analysed CFRP-to-steel bonded joint, the expected interfacial behaviour occurred for a temperature variation between 77.0 °C (FEM) and 77.5 °C (analytical method) which are about 80% lower than the 381 °C estimated for the CFRP-to-steel joint with no influence of T_g at all.

Finally, the authors would like to also recognize that in a real-case situation under very high or low temperatures where materials may dilate or contract significantly, the degradation of hybrid tubular bonded joints can be accelerated due to the introduction of peeling stresses into the debonding process that were ignored in the analytical or numerical models developed in this study. In such cases, the debonding process develops under mixed Mode I&II rather than pure Mode II. Therefore, it would be expected that for a real-case situation, both models may overestimate the maximum temperature from which the integrity of those hybrid tubular joints is compromised, which implies that the proposed closed-form solutions should be used with a rational attitude.

Credit author statement

Hugo C. Biscaia: Conceptualization, Methodology, Investigation, Writing - Original Draft, Visualization, Validation, Supervision, Project administration, Funding acquisition. **Ana P. Martins:** Software, Formal analysis, Investigation, Validation. **Wan-Yang Gao:** Validation, Writing - Review & Editing. **Marta S. Carvalho:** Software, Formal analysis, Validation, Resources, Writing - Review & Editing, Supervision, Funding acquisition.

Declaration of competing interest

The authors declare the following financial interests/personal relationships which may be considered as potential competing interests: Hugo C. Biscaia reports financial support was provided by Foundation for Science and Technology. Marta S. Carvalho reports financial support was provided by Foundation for Science and Technology. Ana P. Martins reports financial support was provided by Foundation for Science and Technology.

Data availability

Data will be made available on request.

Acknowledgements

The authors would like to express their sincere gratitude to Fundação para a Ciência e Tecnologia (FCT) under the strategic project UIDB/00667/2020 (UNIDEMI) and exploratory project EXPL/EME-APL/0994/2021 for providing the funding for this work.

References

Abed, G.M.H., 2012. Effects of Temperature on the Adhesive Bonding in Steel Beams Reinforced with CFRP Composites. PhD Thesis. School of Civil Engineering, Faculty of Engineering and the Environment, University of Southampton.
Ahmeda, G.M.S., Ahmed, H., Mohiuddinc, M.V., Md Sss, 2014. Experimental evaluation of springback in mild steel and its validation using LS-DYNA. Procedia Materials Science 6, 1376–1385.
Al-Shawaf, A.K., 2010. Characterization of Bonding Behavior between Wet-Lay up Carbon Fibre Reinforced Polymer and Steel Plates in Double-Strap Joints under Extreme Environmental Temperatures. PhD Thesis. Department of Civil Engineering, Faculty of Engineering, Monash University.
Al-Shawaf, A., Al-Mahaidi, R., Zhao, X.L., 2006. Study on bond characteristics of CFRP/steel double lap shear joints at subzero temperature exposure. Third International Conference on FRP Composites in Civil Engineering (CICE 2006) (Miami, Florida, USA).
Al-Shawaf, A., Al-Mahaidi, R., Zhao, X.L., 2009. Effect of elevated temperature on bond behaviour of high modulus CFRP/steel double-strap joints. Aust. J. Struct. Eng. 10 (1), 63–74.
Alhassan, M.A., Al-Rousan, R.Z., Taha, H.M., 2020. Precise finite element modelling of the bond-slip contact behavior between CFRP composites and concrete. Construct. Build. Mater. 240, 117943.
Benedyk, J.C., 2010. Aluminum alloys for lightweight automotive structures. Materials, design and manufacturing for lightweight vehicles. In: Woodhead Publishing Series in Composites Science and Engineering. Woodhead Publishing, pp. 79–113.
Biscaia, H.C., 2019. The influence of temperature variations on adhesively bonded structures: a non-linear theoretical perspective. Int. J. Non Lin. Mech. 113, 67–85.
Biscaia, H.C., 2020. Closed-form solutions for modelling the response of adhesively bonded joints under thermal loading through exponential softening laws. Mech. Mater. 148, 103527.
Biscaia, H.C., Chastre, C., 2018. Design method and verification of steel plate anchorages for FRP-to-concrete bonded interfaces. Compos. Struct. 192, 52–66.
Biscaia, H., Diogo, P., 2020. Experimental analysis of different anchorage solutions for laminated carbon fiber-reinforced polymers adhesively bonded to timber. Compos. Struct. 243, 112228.
Biscaia, H.C., Ribeiro, P., 2019. A temperature-dependent bond-slip model for CFRP-to-steel joints. Compos. Struct. 217, 186–205.
Biscaia, H.C., Chastre, C., Silva, M.A.G., 2013a. A smeared crack analysis of reinforced concrete T-beams strengthened with GFRP composites. Eng. Struct. 56, 1346–1361.
Biscaia, H.C., Chastre, C., Silva, M.A.G., 2013b. Modelling GFRP-to-concrete joints with interface finite elements with rupture based on the Mohr-Coulomb criterion. Construct. Build. Mater. 47, 261–273.
Biscaia, H.C., Chastre, C., Silva, M.A.G., 2015a. Bond-slip model for FRP-to-concrete bonded joints under external compression. Compos. B Eng. 80, 246–259.
Biscaia, H.C., Chastre, C., Viegas, A., 2015b. A new discrete method to model unidirectional FRP-to-parent material bonded joints subjected to mechanical loads. Compos. Struct. 121, 280–295.
Biscaia, H.C., Chastre, C., Borba, I.S., Silva, C., Cruz, D., 2016. Experimental evaluation of bonding between CFRP laminates and different structural materials. J. Compos. Construct. 20 (3), 04015070.

Biscaia, H., Chastre, C., Cruz, D., Franco, N., 2017a. Flexural strengthening of old timber floors with laminated carbon fiber reinforced polymers. J. Compos. Construct. 20 (1), 04016073.
Biscaia, H., Chastre, C., Silva, M.A.G., 2017b. Analytical model with uncoupled adhesion laws for the bond failure prediction of curved FRP-concrete joints subjected to temperature. Theor. Appl. Fract. Mech. 89, 63–78.
Bolisetti, C., Whittaker, A.S., Coleman, J.L., 2018. Linear and nonlinear soil-structure interaction analysis of buildings and safety-related nuclear structures. Soil Dynam. Earthq. Eng. 107, 218–233.
Borrie, D., Liu, H.B., Zhao, X.L., Raman, R.K.S., Bai, Y., 2015. Bond durability of fatigued CFRP-steel double-lap joints pre-exposed to marine environment. Compos. Struct. 131, 799–809.
Carvalho, M., Martins, A., Milho, J., 2018. Validation of a railway inline seating model for occupants injury biomechanics. Int. J. Crashworthiness 23 (3), 328–335.
Corcione, C.E., Freuli, F., Frigione, M., 2014. Cold-curing structural epoxy resins: analysis of the curing reaction as a function of curing time and thickness. Materials 7 (9), 6832–6842.
Da Silva, L.F.M., 2010. Improving Bonding at High and Low Temperatures. Advances in Structural Adhesive Bonding. Woodhead Publishing in Materials, Woodhead Publishing, pp. 516–546.
Dai, J.G., Ueda, T., Sato, Y., 2005. Development of the nonlinear bond stress-slip model of fiber reinforced plastics sheet-concrete interfaces with a simple method. J. Compos. Construct. 9 (1), 52–62.
Dai, J.G., Gao, W.Y., Teng, J.G., 2013. Bond-slip model for FRP laminates externally bonded to concrete at elevated temperature. J. Compos. Construct. 17 (2), 217–228.
De Lorenzis, L., Zavarise, G., 2008. Modeling of mixed-mode debonding in the peel test applied to superficial reinforcements. Int. J. Solid Struct. 45, 5419–5436.
Dong, K., Hu, K., 2016. Development of bond strength model for CFRP-to-concrete joints at high temperatures. Compos. B Eng. 95, 264–271.
Doroudi, Y., Fernando, D., Nguyen, V.T., Torres, J.P., 2019. Experimental study on CFRP-to-steel bonded interfaces under quasi-static cyclic loading. J. Compos. Construct. 23 (4), 04019023.
Elsayed, W., Ebead, U.A., Neale, K.W., 2006. Interfacial behavior and debonding failures in FRP-strengthened concrete slabs. J. Compos. Construct. 11 (6), 619–628.
Fernando, D., Yu, T., Teng, J.G., 2014. Behavior of CFRP laminates bonded to a steel substrate using a ductile adhesive. J. Compos. Construct. 18 (2), 04013040.
Ferreira, D., Oller, E., Marí, A., Bairán, J., 2016. Analysis of FRP shear strengthening solutions for reinforced concrete beams considering debonding failure. J. Compos. Construct. 20 (5), 04016018.
Filice, L., Gagliardi, F., Lazzaro, S., Rocco, C., 2010. FE simulation and experimental considerations on TI alloy superplastic forming for aerospace applications. Int. J. Material Form. 3, 41–46.
Focacci, F., Nanni, A., Bakis, C.E., 2000. Local bond-slip relationship for FRP reinforcement in concrete. J. Compos. Construct. 4 (1), 24–31.
Ghafoori, E., Motavalli, M., 2015. Normal, high and ultra-high modulus carbon fiber-reinforced polymer laminates for bonded and un-bonded strengthening of steel beams. Mater. Des. 67, 232–243.
Hallquist, J.O., 2006. LS-dyna Theory Manual. March.
He, J., Xian, G., 2016. Debonding of CFRP-to-steel joints with CFRP delamination. Compos. Struct. 153, 12–20.
He, J., Xian, G., Zhang, Y.X., 2020. Effect of moderately elevated temperatures on bond behaviour of CFRP-to-steel bonded joints using different adhesives. Construct. Build. Mater. 241, 118057.
He, J., Xian, G., Zhang, Y.X., 2021. Numerical modelling of bond behaviour between steel and CFRP laminates with a ductile adhesive. Int. J. Adhesion Adhes. 104, 102753.
Heshmati, M., Haghani, R., Al-Emrani, M., 2017. Durability of bonded FRP-to-steel joints: effects of moisture, de-icing salt solution, temperature and FRP type. Compos. B Eng. 119, 153–167.
Hu, B., Jiang, Y.T., 2019. Comparative study of ultimate bond strength models for FRP-to-steel bonded joints. International Journal of Steel Structures 19, 2051–2072.
Hussain, G., Khan, H.R., Gao, L., Hayat, N., 2013. Guidelines for tool-size selection for single-point incremental forming of an aerospace alloy. Mater. Manuf. Process. 28 (3), 324–329.
Kafkalidis, M.S., Thouless, M.D., 2002. The effects of geometry and material properties on the fracture of single lap-shear joints. Int. J. Solid Struct. 39, 4367–4383.
Khalfallah, S., 2008. Modelling of bond for pull-out tests. Build. Res. J. 56 (1), 37–48.
Klamer, E., 2006. The Influence of Temperature on Concrete Structures Strengthened with Externally Bonded CFRP. Research Report. Eindhoven University of Technology, Netherlands.
Kumar, A.P., Shrivaathsav, S., 2019. Influence of forming parameters on the crash performance of capped cylindrical tubes using LS-DYNA follow-on simulations. Int. J. Interact. Des. Manuf. 13, 1215–1232.
Lam, A.C.C., Cheng, J.J.R., Yam, M.C.H., Kennedy, G.D., 2008. Repair of steel structures by bonded carbon fibre reinforced polymer patching: experimental and numerical study of carbon fibre reinforced polymer – steel double-lap joints under tensile loading. Can. J. Civ. Eng. 34 (12), 1542–1553.
Lee, J., Lopez, M., 2020. Application of frictional bond-slip model to large-scale FRP-strengthened T-beams with U-wraps. International Journal of Concrete Structures and Materials 14 article 1.
Leone, M., Matthys, S., Aiello, M.A., 2009. Effect of elevated service temperature on bond between FRP EBR systems and concrete. Compos. B Eng. 40 (1), 85–93.
Li, S., Thouless, M.D., Waas, A.M., Schroeder, J.A., Zavattieri, P.D., 2006. Mixed-mode cohesive-zone models for fracture of an adhesively bonded polymer-matrix composite. Eng. Fract. Mech. 73, 64–78.
Li, S., Zhu, T., Lu, Y., Li, X., 2016a. Effect of temperature variation on bond characteristics between CFRP and steel plate. International Journal of Polymer Science 8. Article ID 5674572.
Li, S., Zhu, T., Lu, Y., Li, X., 2016b. Effect of temperature variation on bond characteristics between CFRP and steel plate. International Journal of Polymer Science 2016, 8 article ID 5674572.
Li, K., Cao, S., Yang, Y., Zhu, J., 2018a. Bond-slip relationship for CFRP sheets externally bonded to concrete under cyclic loading. Materials 11 (3), 336.
Li, N., Li, S., Liu, C., Zhu, T., 2018b. Bond behavior of CFRP/steel double strap joint at elevated temperatures. https://doi.org/10.20944/preprints201808.0070.v1.
Li, Z., Chen, L., Fang, Q., Chen, W., Hao, H., Zhu, R., Zheng, K., 2019. Experimental and numerical study on CFRP strip strengthened clay brick masonry walls subjected to vented gas explosions. Int. J. Impact Eng. 129, 66–79.
Liu, K., Wu, Y.F., 2012. Analytical identification of bond-slip relationship of EB-FRP joints. Compos. B Eng. 43 (4), 1955–1963.
Liu, H.B., Zhao, X.L., Bai, Y., Singh, R.H., Rizkalla, S., Bandyopadhyay, S., 2014. The effect of elevated temperature on the bond between high modulus carbon fibre-reinforced polymer sheet and steel. Aust. J. Struct. Eng. 15 (4), 355–366.
Lu, X.Z., Teng, J.G., Ye, L.P., Jiang, J.J., 2005. Bond-slip models for FRP sheets/plates bonded to concrete. Eng. Struct. 27, 920–937.
Lu, X.Z., Teng, J.G., Ye, L.P., Jiang, J.J., 2007. Intermediate crack debonding in FRP-strengthened RC beams: FE analysis and strength model. J. Compos. Construct. 11 (2), 161–174.
Luo, H.Y., Zhang, L.L., Zhang, L.M., 2019. Progressive failure of buildings under landslide impact. Landslides 16, 1327–1340.
Lye, H.L., Mohammed, B.S., Wahab, M.M.A., Liew, M.S., 2021. Bond relationship of Carbon Fiber-Reinforced Polymer (CFRP) strengthened steel plates exposed to service temperature. Materials 14 (13), 3761.
Maazoun, A., Matthys, S., Lecompte, D., Belkassem, B., Vantomme, J., 2019. Numerical Modelling of the Debonding between CFRP Strips and Concrete in Shear Tests under Static Loads Using Different Approaches. July. 5th International Conference on Mechanics of Composites, Lisbon, Portugal, pp. 1–4.
Moshiri, N., Czaderski, C., Mostofinejad, D., Hosseini, A., Sanginabadi, K., Breveglieri, M., Motavalli, M., 2020. Flexural strengthening of RC slabs with nonprestressed and prestressed CFRP strips using EBROG method. Compos. B Eng. 201, 108359.
Mostofinejad, D., Shameli, S.M., 2013. Externally bonded reinforcement in grooves (EBRIG) technique to postpone debonding of FRP sheets in strengthened concrete beams. Construct. Build. Mater. 38, 751–758.
Neto, P., Alfaiate, J., Dias-da-Costa, D., Vinagre, J., 2016. Mixed-mode fracture and load misalignment on the assessment of FRP-concrete bond connections. Compos. Struct. 135, 49–60.
Nguyen, T.C., Bai, Y., Zhao, X.L., Al-Mahaidi, R., 2011a. Mechanical characterization of steel/CFRP double strap joints at elevated temperatures. Compos. Struct. 93, 1604–1612.
Nguyen, T.C., Bai, Y., Zhao, X.L., Al-Mahaidi, R., 2011b. Mechanical characterization of steel/CFRP double strap joints at elevated temperatures. Compos. Struct. 93 (6), 1604–1612.
Nguyen, T.C., Bai, Y., Zhao, X.L., Bambach, M.R., Al-Mahaidi, R., 2011c. Temperature effect on adhesively bonded CFRP and steel double strap joints. In: Ye, L., et al. (Eds.), CICE 2010 - the 5th International Conference on FRP Composites in Civil Engineering, vol. 2010. Advances in FRP Composites in Civil Engineering, September 27-29, Beijing, China.
Nozaka, K., Shield, C.K., Hajjar, J.F., 2005. Design of a test specimen to assess the effective bond length of Carbon Fiber-Reinforced Polymer strips bonded to fatigued steel bridge girders. J. Compos. Construct. 9 (4), 304–312.
Pangestuti, E.K., Prihanantio, J., Nuroji, Antonius, 2020. Flexural strength of reinforced concrete beam with CFRP. Malaysian Construction Research Journal 30 article 1.
Qiu, C., Feng, P., Yang, Y., Zhu, L., Bai, Y., 2017. Joint capacity of bonded sleeve connections for tubular fibre reinforced polymer members. Compos. Struct. 163, 267–279.
Rawat, Prashant, Singh, Kalyan Kumar, 2017. An impact behavior analysis of CNT-based fiber reinforced composites validated by LS-DYNA: a review. Polym. Compos. 38 (1), 175–184.
Sahin, M.U., Dawood, M., 2016. Experimental investigation of bond between high-modulus CFRP and steel at moderately elevated temperatures. J. Compos. Construct. 20 (6), 04016049.
Saleh, M.N., Saeedifar, M., Zarouchas, D., De Freitas, S.T., 2020. Stress analysis of double-lap bi-material joints bonded with thick adhesive. Int. J. Adhesion Adhes. 97, 102480.
Salvado, F.C., Tavares, A.J., Teixeira-Dias, F., Cardoso, J.B., 2017. Confined explosions: the effect of compartment geometry. J. Loss Prev. Process. Ind. 48, 126–144.
Shi, J., Zhu, H., Wu, Z., Seracino, R., 2013. Bond behavior between basalt fiber-reinforced polymer sheet and concrete substrate under the coupled effects of freeze-thaw cycling and sustained load. J. Compos. Construct. 17 (4), 530–542.
Siddika, A., Saha, K., Mahmud, S., Roy, S.C., Al-Mamun, A., Alyousef, R., 2019. Performance and failure analysis of carbon fiber-reinforced polymer (CFRP) strengthened reinforced concrete (RC) beams. SN Appl. Sci. 1 article 1617.
Tho, C.H., Sparks, C.E., Sareen, A.K., Smith, M.R., Johnson, C., 2004. Efficient helicopter skid landing gear dynamic drop simulation using LS-DYNA. J. Am. Helicopter Soc. 49 (4), 483–492.
Tvergaard, V., 1990. Effect of fiber debonding in a whisker-reinforced metal. Mater. Sci. Eng. 125, 203–213.
Vaculik, J., Sturm, A.B., Visintin, P., Griffith, M.C., 2018. Modelling FRP-to-substrate joints using the bilinear bond-slip rule with allowance for friction: full-range

analytical solutions for long and short bonded lengths. Int. J. Solid Struct. 135, 245–260.
Valluzzi, M.R., Garbin, E., Modena, C., 2007. Flexural strengthening of timber beams by traditional and innovative techniques. J. Build. Apprais. 3, 125–143.
Van den Bosch, M.J., Schreurs, P.J.G., Geers, M.G.D., 2006. An improved description of the exponential Xu and Needleman cohesive zone law for mixed-mode decohesion. Eng. Fract. Mech. 73, 1220–1234.
Wang, H.T., Wu, G., Dai, Y.T., He, X.Y., 2016. Experimental study on bond behavior between CFRP plates and steel substrates using digital image correlation. J. Compos. Construct. 20 (6), 04016054.
Wenk, J.F., Wall, S.T., Peterson, R.C., Helgerson, S.L., Sabbah, H.N., Burger, M., Stander, N., Ratcliffe, M.B., Guccione, J.M., 2009. A method for automatically optimizing medical devices for treating heart failure: designing polymeric injection patterns. J. Biomech. Eng. 131 (12), 121011.
Wu, Y.F., Jiang, C., 2013. Quantification of bond-slip relationship for externally bonded FRP-to-concrete joints. J. Compos. Construct. 17 (5), 673–686.
Xia, S.H., Teng, J.G., 2005. Behaviour of FRP to steel bonded joints. Proceedings of the International Symposium on Bond Behaviour of FRP in Structures 419–426.
Xiao, X., Botkin, M.E., Johnson, N.L., 2009. Axial crush simulation of braided carbon tubes using MAT58 in LS-DYNA. Thin-Walled Struct. 47 (6–7), 740–749.
Yang, Y., Biscaia, H., Chastre, C., Silva, M.A.G., 2017. Bond characteristics of CFRP-to-steel joints. J. Constr. Steel Res. 138, 401–419.
Yang, Y., Silva, M.A.G., Biscaia, H., Chastre, C., 2018. CFRP-to-steel bonded joints subjected to cyclic loading: an experimental study. Compos. B Eng. 146, 28–41.
Yang, Y., Silva, M.A.G., Biscaia, H., Chastre, C., 2019a. Bond durability of CFRP laminates-to-steel joints subjected to freeze-thaw. Compos. Struct. 212, 243–258.
Yang, Y., Biscaia, H., Silva, M.A.G., Chastre, C., 2019b. Monotonic and quasi-static cyclic bond response of CFRP-to-steel joints after salt fog exposure. Compos. B Eng. 168, 532–549.
Zhao, X.L., Bai, Y., Al-Mahaidi, R., Rizkalla, S., 2014. Effect of dynamic loading and environmental conditions on the bond between CFRP and steel: state-of-the-art review. J. Compos. Construct. 18 (3), A4013005.
Zhou, Y.W., Wu, Y.F., Yun, Y.C., 2010. Analytical modeling of the bond-slip relationship at FRP-concrete interfaces for adhesively-bonded joints. Compos. B Eng. 41 (6), 423–433.
Zhou, H., Urgel, J.M., Emberley, R., Maluk, C., Fernando, D., 2017. Behaviour of the FRP-To-Steel Bonded Joints under Elevated Temperature. 6th Asia-Pacific Conference on FRP in Structures APFIS2017, Singapore.
Zhou, H., Torres, J.P., Fernando, D., Law, A., Emberley, R., 2019. The bond behaviour of CFRP-to-steel bonded joints with varying bond properties at elevated temperatures. Eng. Struct. 183, 1121–1133.
Zhou, H., Fernando, D., Torero, J.L., Torres, J.P., Maluk, C., Emberley, R., 2020. Bond behavior of CFRP-to-steel bonded joints at mild temperatures: experimental study. J. Compos. Construct. 24 (6), 04020070.
Zhu, M., Ueda, T., Zhu, J.H., 2020. Generalized evaluation of bond behavior of the externally bonded FRP reinforcement to concrete. J. Compos. Construct. 24 (6), 04020066.